Journal of Asian Earth Sciences 196 (2020) 104364

Contents lists available at ScienceDirect

Journal of Asian Earth Sciences

journal homepage: www.elsevier.com/locate/jseaes

Intraplate adakite-like rocks formed by differentiation of mantle-derived mafic magmas: A case study of Eocene intermediate-felsic porphyries in the Machangqing porphyry Cu-Au mining district, SE Tibetan plateau

Ying-Jing Wang[a,b], Xin-Song Wang[a,*], Xian-Wu Bi[a], Yan Tao[a], Ting-Guang Lan[a]

[a] State Key Laboratory of Ore Deposit Geochemistry, Institute of Geochemistry, Chinese Academy of Sciences, Guiyang 550081, PR China
[b] University of Chinese Academy of Sciences, Beijing 100049, PR China

ARTICLE INFO

Keywords:
Adakite-like rocks
Intraplate setting
Clinopyroxene antecrysts
High-Al amphiboles
Western Yangtze Craton

ABSTRACT

Intraplate intermediate-felsic adakite-like rocks are widely considered to be generated via partial melting of the mafic lower crust. However, the genesis of phenocrysts of mafic minerals from some adakite-like rocks suggests that they can originate from mantle-derived magmas through assimilation and fractional crystallization (AFC) processes. In this study, we investigated the petrogenesis of three phases of Eocene porphyries, namely quartz diorite porphyry (QDP-I and QDP-II), granodiorite porphyry (GDP), and granite porphyry (GP), exposed in the Machangqing area of the western Yangtze Craton in the southeastern Tibetan plateau. These porphyries were formed at 34.2–35.2 Ma in an intracontinental extension setting and present adakitic affinities of high Sr/Y (50–95) and La/Yb (50–113) ratios. The similar characteristics of these Machangqing porphyries in terms of whole-rock trace elements and Sr–Nd isotopes, as well as in the mineralogy of amphibole phenocrysts and clinopyroxene antecrysts, indicate that these intermediate-felsic porphyries were derived from the same source. The important observation for investigating the parental magma of these intermediate-felsic porphyries is that they have close temporal and spatial correlations with mantle-derived mafic volcanic rocks. These intermediate-felsic porphyries have slightly enriched Sr–Nd isotopic compositions [$(^{87}Sr/^{86}Sr)_i$ = 0.7068–0.7077, εNd (t) = −5.1 to −6.6], affected by limited crustal assimilation, as compared to those of contemporaneous mafic volcanic rocks. The high-Al amphibole phenocrysts and clinopyroxene antecrysts in QDP-I have similar rare earth element (REE) patterns with clinopyroxene phenocrysts in the mafic volcanic rocks, which suggest that these rocks originated from the same mantle-derived mafic magma. In addition, the major elements of these intermediate-felsic and mafic igneous rocks in the Machangqing area show fractional crystallization trends with an increasing magma silica component. Simulations of the major and trace elements of these igneous rocks show that the sequence of fractional crystallization of olivine, clinopyroxene, garnet, amphiboles, biotite, feldspar, and apatite with time promoted the evolution of the magma series. As revealed by the calculated physicochemical conditions during crystallization of the phenocrysts, the initial mafic magmas were derived from depths of greater than 64 km through the partial melting of the metasomatic lithosphere mantle induced by Eocene intraplate extension in the western Yangtze Craton. These initial mafic magmas underwent three stages of fractional crystallization at three levels of the thickened crust: the first at the base of the lower crust (49–55 km); followed by fractional crystallization at the middle crust (24–32 km); and finally at the upper crust (4–5 km). These fractional crystallization processes caused the initial mafic magmas to evolve through the intermediate (roughly represented by QDP-I) to the felsic compositions (GDP and GP). Whole-rock and mineral geochemistry evidence demonstrates that fractional crystallization of mantle-derived magmas, with a small amount of crustal assimilation, generated these Eocene intraplate intermediate-felsic adakitic porphyries in the Machangqing area.

1. Introduction

Typical adakite is a kind of igneous rocks in oceanic islands, generated from the partial melting of subducted young (≤25 Ma) and hot oceanic slabs (Defant and Drummond, 1990). Other igneous rocks formed in continental arcs and intraplate settings can exhibit geochemical signatures similar to those of adakite, i.e., Sr/Y ≥ 20, La/Yb ≥ 20, Y ≤ 28 ppm, and Yb ≤ 1.9 ppm, and are thus described as

* Corresponding author.
E-mail addresses: yingjwang@126.com (Y.-J. Wang), wangxinsong@mail.gyig.ac.cn (X.-S. Wang).

https://doi.org/10.1016/j.jseaes.2020.104364
Received 4 November 2019; Received in revised form 8 April 2020; Accepted 8 April 2020
Available online 13 April 2020
1367-9120/

"adakite-like" rocks (Castillo et al., 1999; Defant and Drummond, 1993; Richards and Kerrich, 2007). Two primary models have been proposed for the genesis of adakite-like rocks: (1) partial melting of the mafic lower crust (Hou et al., 2004; Ren et al., 2018; Wang et al., 2006, 2014a; Xu et al., 2002) and (2) partial melting of the metasomatic lithospheric mantle followed by assimilation and fractional crystallization (AFC) processes (Macpherson et al., 2006; Ribeiro et al., 2016; Wang et al., 2019b). However, the latter is rarely proposed as the genesis model for the intraplate adakite-like rocks (Chen et al., 2013; Ma et al., 2016).

Phenocrysts of mafic minerals in porphyries or volcanic rocks commonly crystallize in the deep magma chamber. Because magmas of porphyries or volcanic rocks usually ascend to the upper crust abruptly and cool quickly, these phenocrysts can record abundant information on the magma petrogenesis (Cao et al., 2018a, 2018b; Tang et al., 2017). The chemical compositions of these phenocrysts can be used to calculate the physicochemical conditions of equilibrated magmas (Purika et al., 2003; Ridolfi and Renzulli, 2012; Zhang et al., 2017). Combined with their host rocks' geochemistry, these phenocrysts can shed light on the magma source and magma evolution process (Barnes et al., 2017; Wang et al., 2019a).

In the western margin of the Yangtze Craton in the southeastern (SE) Tibetan plateau, Eocene intermediate-felsic porphyries in the Machangqing porphyry Cu-Au mining district are distributed closely with contemporaneous potassic-ultrapotassic mafic volcanic rocks (Figs. 1a and 2a). Previous studies have proposed that these Eocene potassic–ultrapotassic mafic volcanic rocks are generated from the partial melting of metasomatic mantle (Guo et al., 2005; Huang et al., 2010), whereas Eocene Machangqing porphyries showing adakitic affinities are derived from the partial melting of juvenile mafic lower crust (Lu et al., 2013). However, given the close temporal and spatial relationships between the Eocene mafic volcanic rocks and the intermediate-felsic porphyries, there is a possibility that the intermediate-felsic porphyries were formed by differentiation of the mantle-derived mafic magma.

In this study, we investigated the petrogenesis of quartz diorite porphyries (QDP-I and QDP-II), granodiorite porphyry (GDP), and granite porphyry (GP) in the Machangqing porphyry Cu-Au mining district through analysis of zircon U–Pb ages, whole-rock major and trace elements, and Sr–Nd isotopes. We also analyzed the major and trace elemental compositions of amphiboles and clinopyroxenes in these porphyries. Combined with the results of comparison, in terms of the whole-rock geochemistry and mineralogy, between Machangqing intermediate-felsic porphyries and these contemporaneous mantle-derived mafic volcanic rocks and lower crustal xenoliths (representing the juvenile mafic lower crust) in the same area, we propose that intermediate-felsic porphyries in the Machangqing area are adakite-like rocks that were generated by differentiation of mantle-derived magma through AFC processes in an intraplate setting during the Eocene.

2. Geological background

The northern part of the Yangtze Craton is separated from the North China Craton by the Qinling-Dabie orogenic belt and is adjacent to the Qiangtang and Songpan-Ganzi blocks of the Tibetan plateau (Fig. 1a). It is bounded to the west by the Ailao Shan-Red River shear zone (ASRRS) (Fig. 1b). The Yangtze Craton has an Archean (2.87–3.00 Ga) basement (Gao et al., 1999). It experienced significant cratonization during the Proterozoic (Chen and Jahn, 1998; Li et al., 2014). The earliest evidenced oceanic subduction in the area occurred in the Neoproterozoic (864–760 Ma), and mafic and felsic rocks of this period are widely distributed along the western and northern edges of the Yangtze Craton (Zhao et al., 2019; Zhou et al., 2002). After the Neoproterozoic to Triassic transition, the western Yangtze Craton was covered by thick sequences of strata comprising glacial deposits and clastic, carbonate, and meta-volcanic rocks (Zhou et al., 2002). During the Late Permian (259–260 Ma), the western Yangtze Craton was disturbed by the Emeishan mantle plume and covered by basalt formations of the Emeishan large igneous province (Chung and Jahn, 1995; He et al., 2003; Zhong et al., 2011). During the late Permian to Triassic (~220 Ma), the westward subduction of the Jinsha Jiang-Ailao Shan ocean basin to the Simao block (Wang et al., 2000), together with the closure of the Songpan-Ganzi ocean basin (Leng et al., 2014; Wang et al., 2019b), made the western Yangtze Craton an intraplate setting.

During the Late Cretaceous to Early Cenozoic, at approximately 70–55 Ma, following the closure of the Neo-Tethys Ocean, the northeastward-moving Indian plate collided with the Eurasian plate (Chung et al., 2005; Wang et al., 2014b, 2019c). At ~40 Ma, the direction of the movement of the Indian plate changed from northeastward to northward, followed by clockwise rotation (Fig. 1c and d; Replumaz et al., 2014; Xu et al., 2016b). This rotation resulted in the southeastward extrusion of the Indochina block starting at 41 Ma (Xu et al., 2016a) and the generation of the ASRRS (Peltzer and Tapponnier, 1988). The change in tectonic activity was simultaneous with the beginning of Eocene magmatism (40–42 Ma) in the western Yangtze Craton (Fig. 1e; Lu et al., 2012; Xu et al., 2012). A sinistral shear motion of the ASRRS occurred at approximately 30–27 Ma (Chung et al., 1997; Tang et al., 2013). Before the sinistral motion, large amounts of Eocene-Oligocene mafic and intermediate-felsic intrusions (associated with Cu–Au–Mo deposits) were emplaced in the western Yangtze Craton at 43–30 Ma (Fig. 1b and e; Bi et al., 2000, 2009; Guo et al., 2005; Liang et al., 2007).

Several kinds of crustal xenoliths have been found enclosed in these Eocene-Oligocene intermediate-felsic intrusions (Hou et al., 2017; Liu et al., 1999; Zhou et al., 2017). Among these crustal xenoliths, garnet pyroxenite, garnet amphibole-pyroxenite, and garnet amphibolite in the Liuhe aegirine syenite porphyry were proposed to be xenoliths from the juvenile mafic lower crust (Zhou et al., 2017). The juvenile mafic lower crust has been suggested to be the product of mantle-derived material generated through Neoproterozoic oceanic subduction and Late Permian plume-lithosphere interaction (Zhou et al., 2017). The initial Sr–Nd isotopic composition of these lower crustal xenoliths at 36 Ma is $^{87}Sr/^{86}Sr$ = 0.7069–0.7088 and εNd (t) from −5.4 to 1.1 (Zhou et al., 2017). The clinopyroxenes in the lower crustal xenoliths have elemental characteristics of $Mg^{\#}$ = 45–86 ($Mg^{\#}$ = 100 * [Mg/(Mg + Fe)]), Al_2O_3 = 0.52–8.15 wt%, TiO_2 = 0.11–0.69 wt%, Na_2O = 0.28–2.59 wt%, and Ti/Al = 0.03–0.27 (Wei and Wang, 2004; Zhao et al. 2003; Zhou et al., 2017). The results calculated using a garnet–clinopyroxene Fe–Mg geothermometer revealed that these xenoliths were captured from the juvenile mafic lower crust at a corresponding depth of 45–51 km (Zhou et al., 2017).

3. Regional geology

The Machangqing porphyry Cu–Au deposit is located at the western edge of the western Yangtze Craton and has reserves of 39 Mt Cu and ~12 t Au (Hou et al., 2006). Re–Os dating of these ore bodies and U-Pb ages of titanite in the mineralized skarn showed that the mineralization formed at 34–36 Ma (Fu et al., 2018; Hou et al., 2006; Xu et al., 2012). The Cu and Au mineralization are mainly distributed in the Baoxingchang and Rentouqing sections as veinlets (Fig. 2b; Bi et al., 2009; Hou et al., 2006). The He, Ar, S, and C isotopic compositions of the ore-forming fluids suggest that the mineralization of Cu and Au is genetically associated with intermediate-felsic porphyries in the area (Bi, 1999, Bi et al., 2000; Hu et al., 1998, 2004). Outcrops of these intermediate-felsic porphyries in Machangqing present a nearly oval-shaped zonation (Fig. 2b). From exterior to interior, the sequence comprises three phases—quartz diorite porphyry (QDP), granodiorite porphyry (GDP), and granite porphyry (GP). These porphyries intrude into the Ordovician clastic rocks and Devonian limestones (Fig. 2b). The intercalating relationships observed are shown in the profile in Fig. 3a and the hand specimens are shown in Fig. 3b–e. Based on our fieldwork

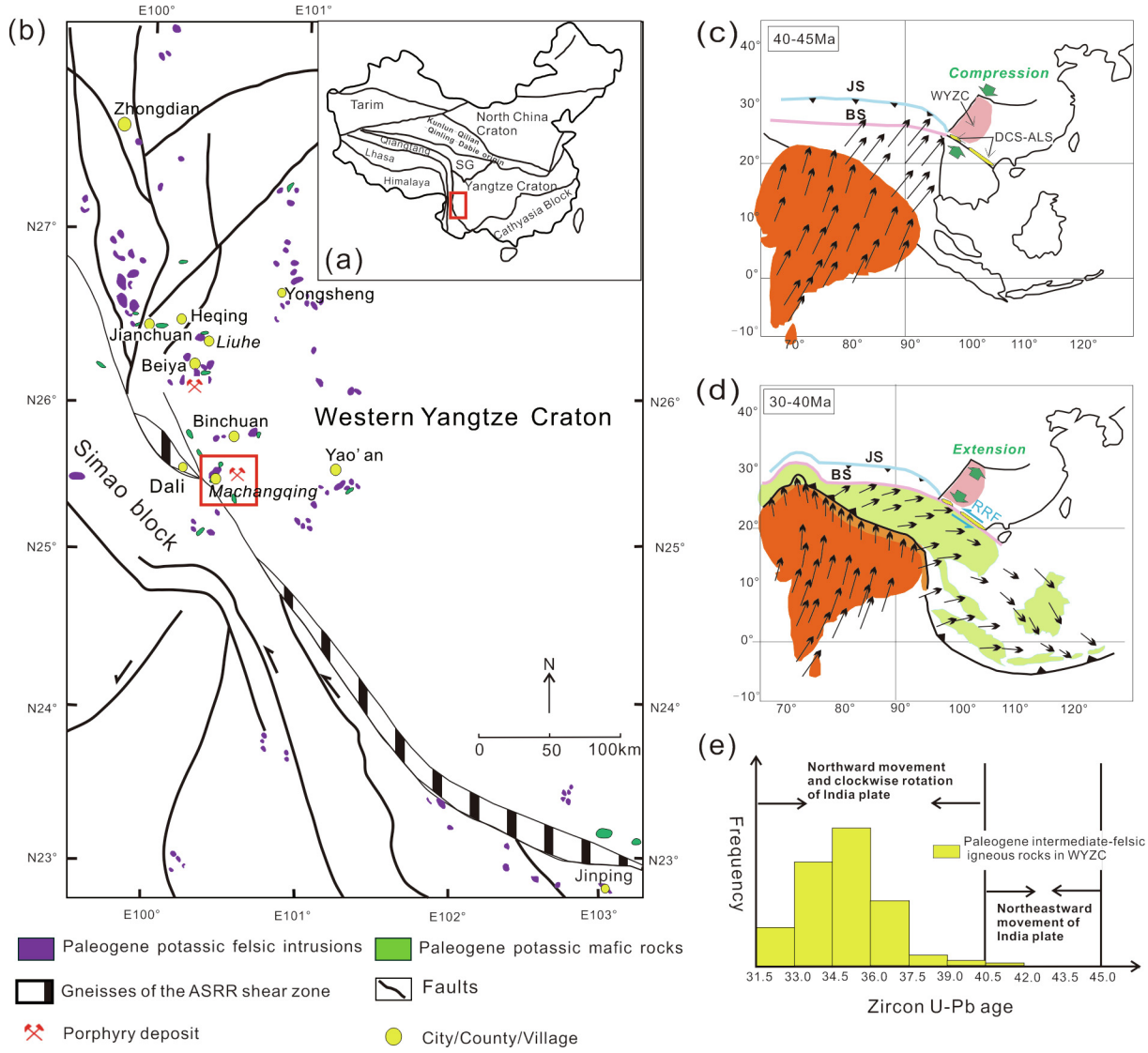

Fig. 1. (a) Tectonic subdivisions of China; SG, Songpan-Ganzi block. (b) Simplified geological map of the western Yangtze Craton (modified after Huang et al., 2010); ASRR, Ailao Shan-Red River. (c–d) Tectonic reconstructions in South Asia at 40–45 Ma and 30–40 Ma, respectively (modified after Replumaz et al., 2014); WYZC, western Yangtze Craton; RRF, Red River faults; JS, Jinsha sutures; BS, Bangong sutures; DCS-ALS, Diancang Shan-Ailao Shan. (e) Histogram of Zircon U–Pb ages of Paleogene intermediate-felsic igneous rocks in the western Yangtze Craton (data from Lu et al., 2012).

observations, the QDP is divided into two groups, dark gray QDP-I and green QDP-II (Fig. 3b and c). The widely exposed QDP in the deposit area is QDP-I. GP intrudes into and cuts across GDP (Fig. 3a). QDP-II cuts across other porphyries as veins (Fig. 3a).

The potassic–ultrapotassic mafic volcanic rocks are exposed along faults in the Machangqing area (Fig. 2a). Previous studies propose that these mafic volcanic rocks were generated at 36.6–35.5 Ma and derived from a metasomatic mantle source (Guo et al., 2005; Huang et al., 2010; Xu et al., 2003). In a study by Huang et al. (2010), the chemistry of the mafic rocks present distinck characteristics, e.g., from basaltic to andesitic (SiO_2 = 44.48–59.05 wt%, MgO = 6.24–21.82 wt%), high La_N/Yb_N (average 11.6), and enriched Sr–Nd isotopic signatures ($^{87}Sr/^{86}Sr$ = 0.7056–0.7065, εNd(t) = −4.36 to −0.97). And the mafic volcanic rocks mainly contain phenocrysts of olivine and clinopyroxene. The primary phenocrysts of clinopyroxenes in the mafic volcanic rocks show complex zoning textures, e.g., normal, reverse, and oscillatory zonings. The primary clinopyroxene phenocrysts show features of $Mg^{\#}$ = 77–90, Ti/Al = 0.06–0.16, Al_2O_3 = 0.73–1.68 wt%, TiO_2 = 0.13–0.29 wt%, and Na_2O = 0.22–0.42 wt%. Rare earth element patterns of these clinopyroxenes show convex upward shapes.

4. Petrology

4.1. Intermediate-felsic porphyries in Machangqing

As mentioned earlier, three phases of intermediate-felsic porphyries are exposed in the Machangqing area, namely QDP (QDP-I and QDP-II), GDP, and GP. QDP-I has a porphyritic texture (Figs. 3b and 4a–c) and contains approximately 40% phenocrysts, including ~15% amphibole, ~10% plagioclase, ~5% quartz, ~5% biotite, and < 5% alkali feldspar. The accessory minerals are apatite, allanite, titanite, zircon, and magnetite. Clinopyroxene antecrysts observed in QDP-I occur as euhedral clusters with disequilibrium structures such as colorless cores and green tattered rims (Fig. 4a), or are enclosed in amphiboles (Fig. 4b). Two types of amphibole phenocrysts occur in QDP-I, namely AmpI (high-Al amphibole, length < 1 mm) and AmpII (low-Al amphibole, length > 1 mm) (Fig. 4c). AmpI has a significant zoned texture (Fig. 4b), whereas AmpII shows twinning and weak zoned textures (Fig. 4c). AmpI and AmpII exhibit light-green to dark-green polychroism. The quartz phenocrysts are euhedral with rounded corners. The mineral assemblage in QDP-II is slightly different from that in QDP-I. The

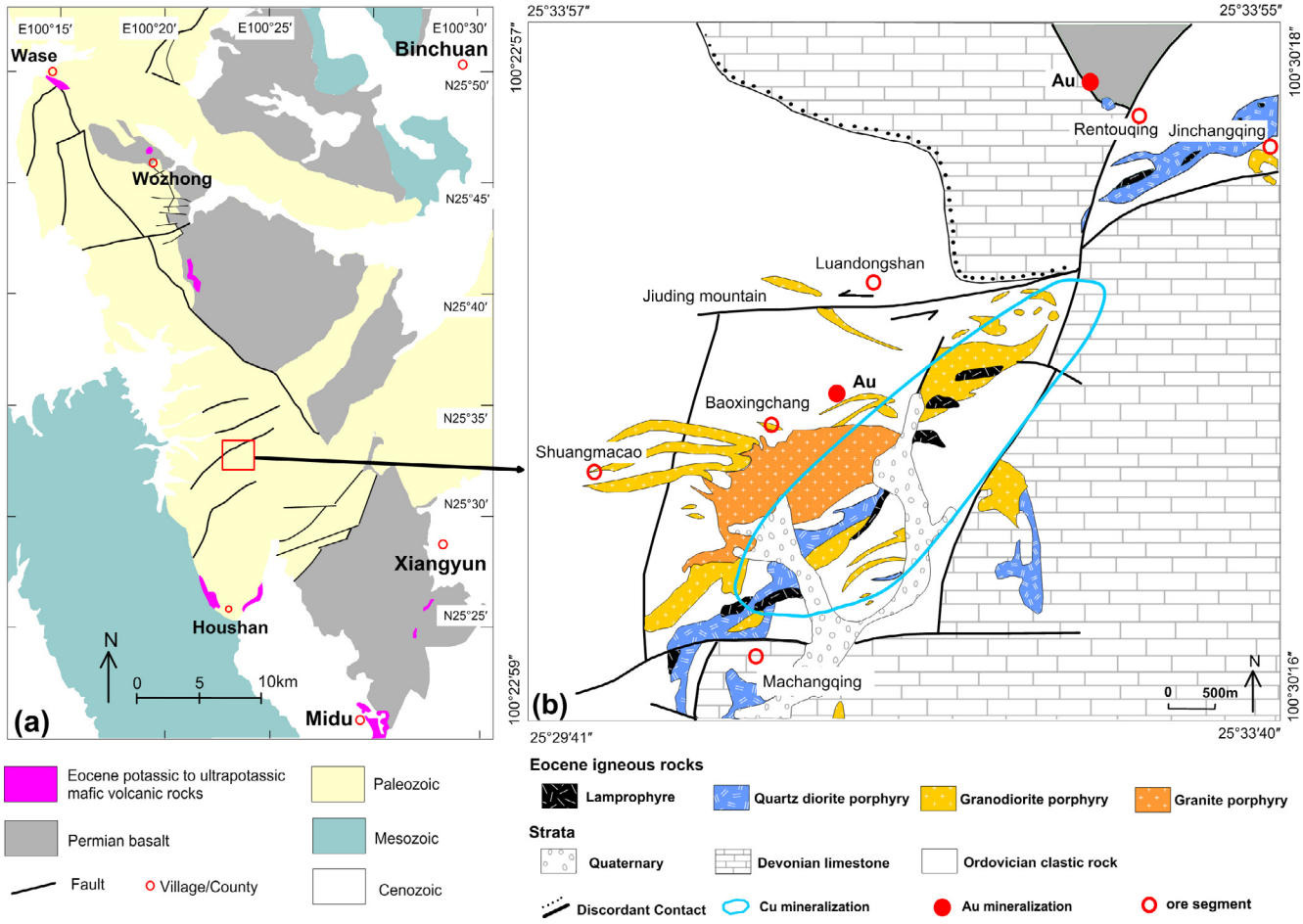

Fig. 2. Simplified geological map showing (a) distribution of Eocene mafic volcanic rocks near Machangqing (modified after Huang et al., 2010) and (b) distribution of Machangqing Eocene intermediate-felsic porphyries and Au-Cu mineralization areas (modified after Yu, 1988; Hou et al., 2006).

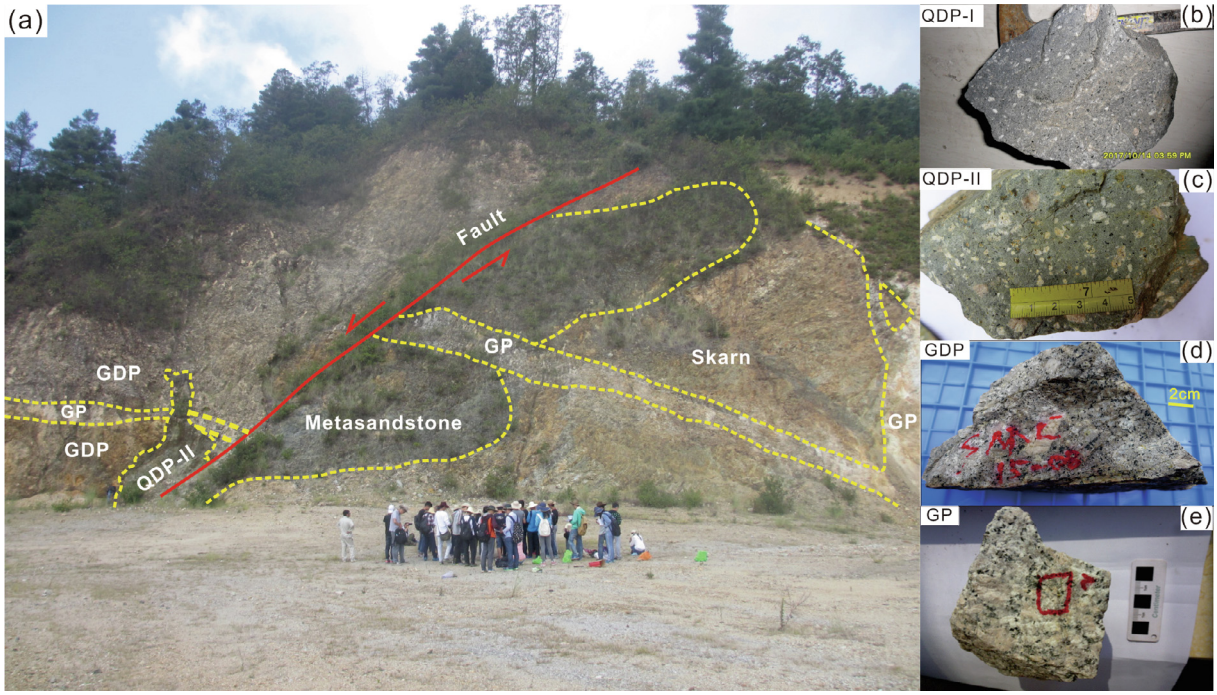

Fig. 3. (a) Field profile photographs, and (b–e) Hand specimens of intermediate-felsic porphyries in Machangqing. The intermediate porphyry is quartz diorite porphyry (QDP-I and QDP-II). The felsic porphyries are granodiorite porphyry (GDP) and granite porphyry (GP).

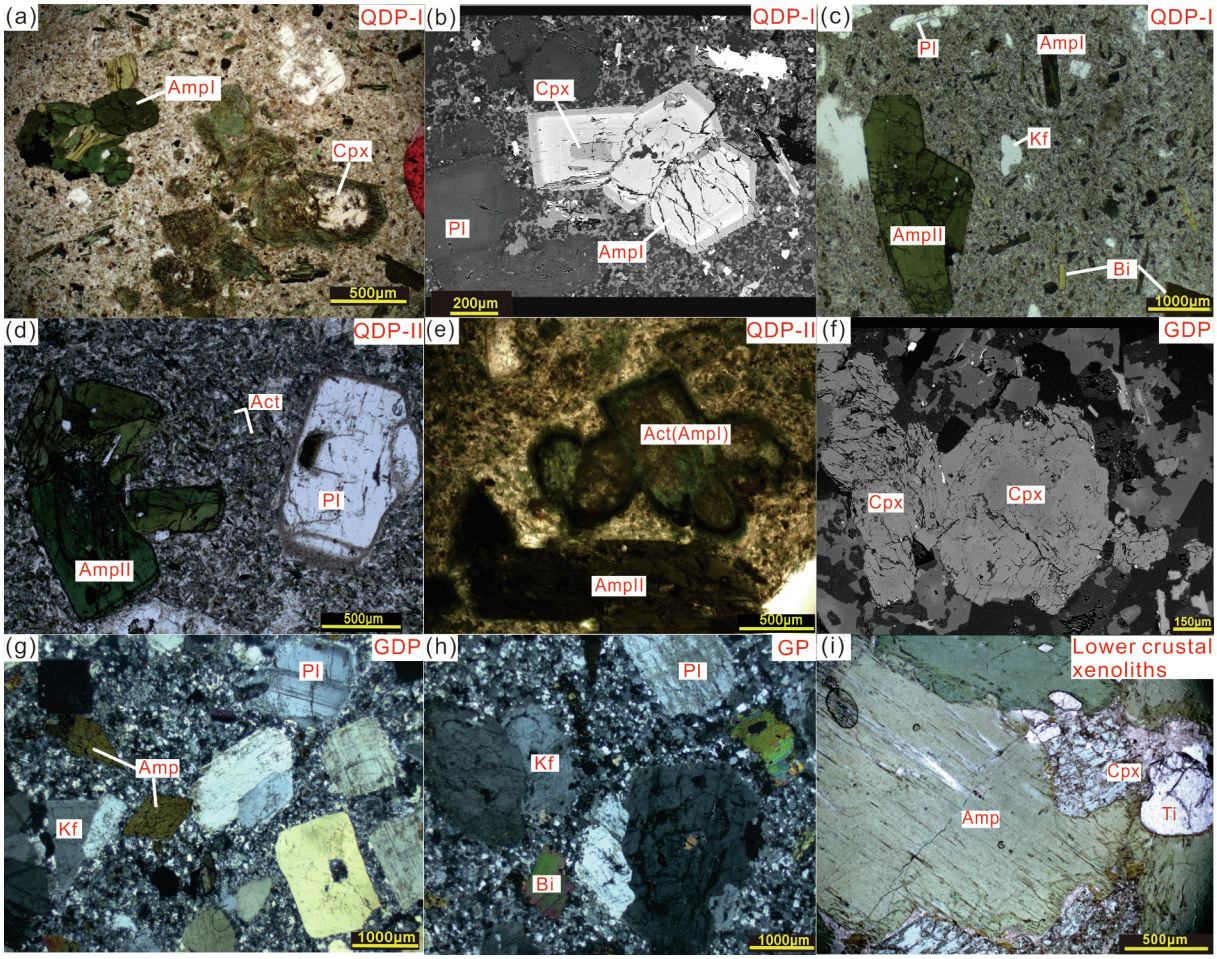

Fig. 4. Photomicrographs of (a–h) intermediate-felsic porphyries in Machangqing, and (i) lower crustal xenoliths from Liuhe. (b) and (f) are backscattered electron images and the others are optical microscope images. Pl, plagioclase; Amp, amphibole; Kf, alkali feldspar; Bi, biotite; Cpx, clinopyroxene; Ti, titanite; Act, actinolite.

plagioclase and AmpII in QDP-II are fresh-looking and seem identical to those in QDP-I (Fig. 4d). However, AmpI converts to actinolite with minor conversions of chlorite (Fig. 4e), and actinolite is the primary mafic mineral in the matrix of QDP-II (Fig. 4d and e). Thus, the hand sample of QDP-II appears green (Fig. 3c).

Clinopyroxene antecrysts are also found in GDP and GP, but they are cracked (Fig. 4f). GDP has a porphyritic texture (Figs. 3d and 4g) and is made up of approximately 50% phenocrysts, including 15% plagioclase, 10% quartz, 10% alkali feldspar, 10% amphiboles, and 5% biotite. GDP has more amphibole phenocrysts than biotite, whereas the opposite is observed for GP. GP shows a porphyraceous texture (Figs. 3e and 4h) and is composed of phenocrysts of approximately 20% alkali feldspar, 15% plagioclase, 15% quartz, 5% biotite, and 5% amphiboles. The matrix is made up of 25% alkali feldspar, and 15% quartz. Amphibole phenocrysts in GDP and GP exhibit light to dark claybank polychroism. The accessory minerals in GDP and GP are apatite, titanite, allanite, zircon, and magnetite.

4.2. Lower crustal xenoliths

In this work, we investigated the geochemistry of amphiboles and clinopyroxene in the lower crustal garnet amphibolite xenoliths (Fig. 4i) enclosed in Liuhe porphyries in the western Yangtze Craton (Fig. 1b). In these garnet amphibolite xenoliths, amphiboles (~65%) are anhedral, with large grain sizes of 0.4–3 mm. Clinopyroxenes (~30%) have an anhedral, round shape with grain sizes of 0.2–1 mm, and they are surrounded by amphiboles (Fig. 4g). Garnets (~5%) are smaller in size (0.2–0.5 mm). The accessory minerals are apatite, titanite, and zircon.

5. Analytical methods

5.1. Zircon U–Pb dating

Zircon grains were separated from their host rocks by standard density and magnetic concentration techniques. Zircon grains of similar size were cast with epoxy into cylinders and polished down until the zircon cores were nearly reached. To select dating spots without inclusions or cracks, zircon grains were imaged using both reflected and transmitted illumination schemes in optical microscopy. Cathodoluminescence (CL) images were taken using a JSM 7800F thermal field emission scanning electron microscope equipped with a CL instrument (MonoCL4) at the State Key Laboratory of Ore Deposit Geochemistry (SKLODG), Institute of Geochemistry, Chinese Academy of Sciences, Guiyang, China. U–Pb dating and trace-element analysis were performed simultaneously using laser ablation inductively coupled plasma mass spectrometry (LA-ICP-MS) at SKLODG. Laser sampling was operated with a Geolas Pro excimer laser ablation system, and ion-signal intensities were acquired with an Agilent 7900 ICP-MS instrument. The diameter of the sampling spots was 32 μm, and the energy density and sampling frequency of the laser beams were 8 J/cm^2 and 6 Hz, respectively. Each analysis consisted of 18–20 s of background acquisition and 50 s data acquisition. Detailed operating conditions were based on previous studies (Liu et al., 2010a, 2010b). The external standard sample used for U–Pb age calibration was 91500. The GJ was used as a secondary standard sample. Every eighth zircon

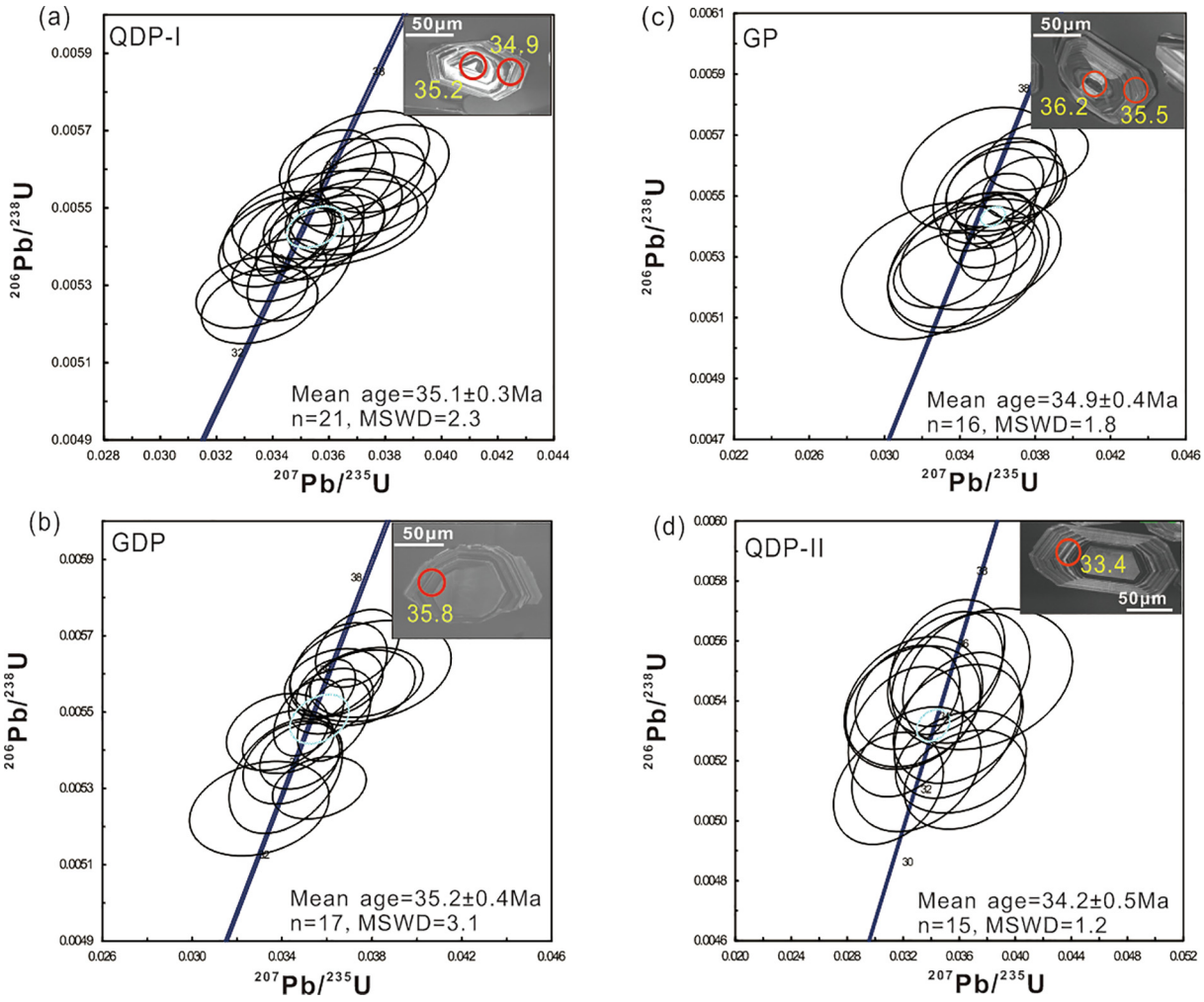

Fig. 5. U–Pb ages and cathodoluminescence (CL) images of zircons from intermediate-felsic porphyries in Machangqing. In the zircon CL images, sampling dots and their U–Pb ages are labeled.

sample analysis was followed by duplicate analyses of the 91500 standard samples. And every sixteenth zircon sample analysis was followed by a single GJ analysis. The standard $^{238}U/^{206}Pb$ age of GJ obtained by LA-ICP-MS is 610 ± 1.7 Ma (Elhlou et al., 2006). The standard error of the calibrated $^{238}U/^{206}Pb$ ages of GJ in this work was better than 10%. Off-line choice and calculation of obtained signals were performed by ICPMSDataCal 10 (Liu et al., 2010a, 2010b). Concordia diagrams and weighted average ages were calculated using the ISOPLOT 3.23 program of Ludwig (2001).

5.2. Whole-rock major and trace elements

Twelve fresh or weakly altered rocks were cleaned with water. After drying, they were crushed and ground to powder (< 75 μm) in a corundum mill. Fused borate–lithium nitrate glass pellets were prepared and analyzed using a PANalytical Axios-advance X-ray fluorescence (XRF) spectrometer at the ALS Laboratory Group, Guangzhou, China. Analytical precision was generally better than 5%. Trace elements were analyzed with the Perkin-Elmer ELAN DRC-e ICP-MS instrument at SKLODG. After the addition of a mixture of HF and HNO_3, 50 mg of powder was dissolved in Teflon-lined stainless-steel bombs and maintained at ~190 °C for two days. Before analysis, an internal Rh (rhodium) standard was incorporated into all samples to monitor signal drift during analysis. Detailed analytical methods were described by Qi et al. (2000). The analytical precision was generally better than 10%.

5.3. Whole-rock Sr–Nd isotopes

Chromatographic separation of Sr and Nd was performed at the Key Laboratory of Crust-Mantle Materials and Environments, University of Science and Technology of China. Sample preparation and Sr and Nd isotope analyses followed procedures described by Chen et al. (2005). Sr and Nd isotope analyses were carried out on a Thermo Fisher Scientific Neptune plus MC-ICP-MS at SKLODG. During the analytical session, the Sr standard reference material NBS 987 was analyzed every 10 samples to monitor the quality of the analysis. Replicate analysis of this reference material yielded $^{87}Sr/^{86}Sr$ = 0.710259 ± 11 (2SD, n = 6), which matched the recommended value of 0.710248. The $^{87}Sr/^{86}Sr$ ratio was normalized to the $^{86}Sr/^{88}Sr$ ratio using the exponential law. During Nd isotope analysis, repeated measurement of JNdi-1 standard yielded $^{143}Nd/^{144}Nd$ = 0.512112 ± 11 (2SD, n = 8), which matched the recommended value of 0.512115. Nd isotope ratios were internally corrected for mass fractionation using a constant value of 0.7219 for $^{146}Nd/^{144}Nd$ by the exponential law. Total procedural blanks were approximately 30 pg Sr and 25 pg Nd. The $^{87}Rb/^{86}Sr$ and $^{147}Sm/^{144}Nd$ ratios were calculated using the whole-rock concentrations of Rb, Sr, Sm, and Nd obtained by ICP-MS.

5.4. Mineral geochemistry

The major elemental compositions of the amphiboles and clinopyroxenes were obtained by electron probe microanalysis (EPMA) at

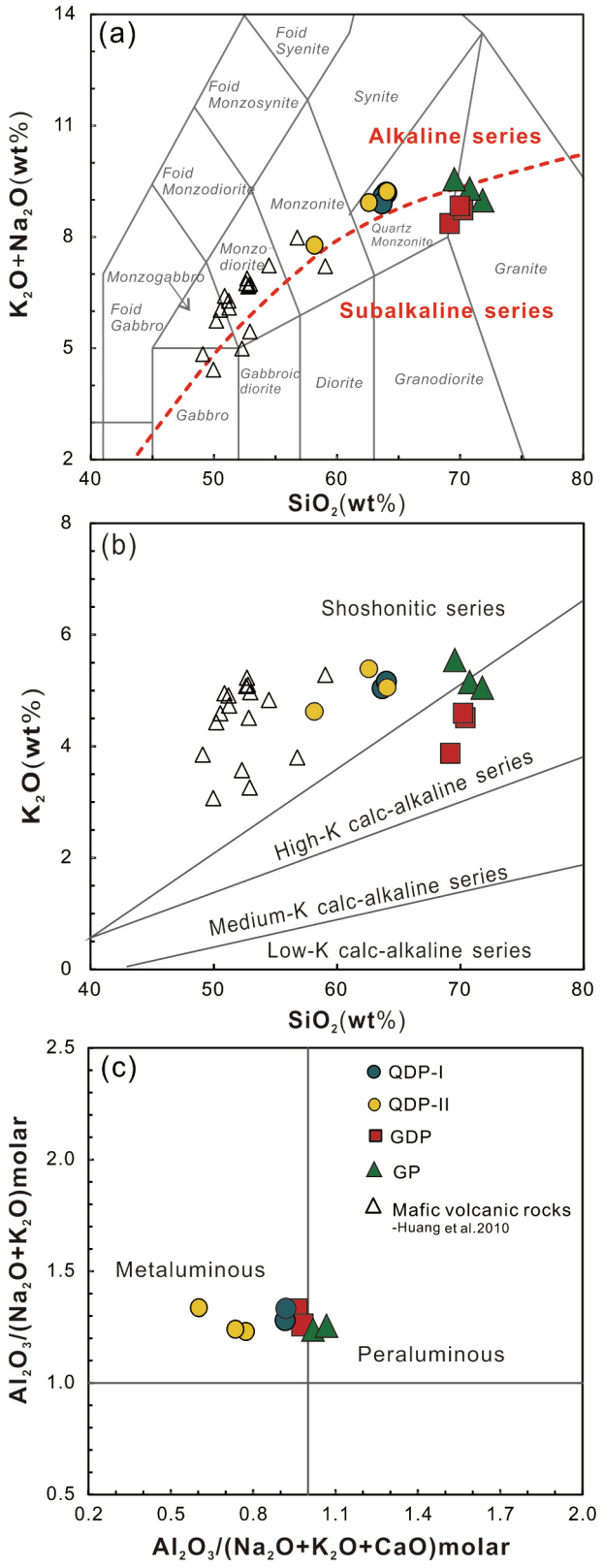

Fig. 6. (a) Total alkali vs. silica diagram (Irvine and Baragar, 1971; Middlemost, 1994); (b) K_2O vs. SiO_2 diagram (modified after Rickwood, 1989); and (c) molar $Al_2O_3/(Na_2O + K_2O)$ vs. molar $Al_2O_3/(CaO + Na_2O + K_2O)$ diagram of Eocene Machangqing intermediate-felsic porphyries and mafic volcanic rocks. Data for the Eocene mafic volcanic rocks are from Huang et al. (2010).

two different laboratories using natural and synthetic standards. Matrix effects were corrected for using the ZAF software. The major element contents of amphiboles and clinopyroxenes in the Machangqing porphyries, listed in Tables C2 and C4, were determined using a JEOL JXA-8230 electron probe microscopic analyzer at The Testing Center of Shandong Bureau of China Metallurgy and Geology, Jinan, China. Typical operating conditions were an accelerating voltage of 15 kV, a beam current of 20 nA, and a spot size of 5 μm. The major elements of amphiboles used for internal standard calibration of LA-ICP-MS analyses were obtained at SKLODG using an EPMA-1600 instrument. Analytical conditions included an accelerating voltage of 25 kV and a beam current of 10 nA, focusing on 10-μm-diameter spots.

Trace element analyses of the amphiboles and clinopyroxenes on polished sections were carried out using a GeolasPro 193 nm solid-state laser system coupled with an Agilent 7900 ICP-MS at SKLODG. Obvious inclusions in the amphiboles and clinopyroxenes were avoided using plane-polarized light before LA-ICP-MS analysis. Operating conditions consisted of 32 μm diameter spots and a laser pulse rate of 5 Hz. For each analysis, 18 s background and 50 s signal acquisitions were adopted. The analytical standard, NIST610 glass, was analyzed after every sixth unknowns. Precision was determined by repeated analysis of standard basaltic glass 3B series (BHVO-2G, BCR, BIR). The accuracy relative to standard basaltic glass was better than 10%. The trace element contents of hydrous amphiboles were normalized using CaO contents (wt%) obtained by EPMA as internal standards. Trace element contents of anhydrous clinopyroxenes were calculated by applying the ablation yield correction factor (AYCF) and using the standard basaltic glass 3B series as multiple reference materials without applying internal standardization (Liu et al. 2008). Off-line selection and integration of analysis signals, time-drift correction and quantitative calibration were performed using ICPMSDataCal 10 (Liu et al., 2010a, 2010b).

5.5. Calculations of physicochemical conditions

The physicochemical conditions of the equilibrated mafic magmas were preliminarily calculated using clinopyroxene-liquid thermobarometry (Purika et al., 2003). The Excel files used in the calculations were referenced from Hu et al. (2018).

The geochemical compositions of the groundmass were regarded as the compositions of the melt equilibrated with phenocrysts (Dahren et al., 2012). The equilibrated melt during crystallization of clinopyroxene phenocrysts in the mafic volcanic rocks was determined by mass balance calculations based on the major element contents of the bulk rocks and the phenocrysts of olivine and clinopyroxene (Huang et al., 2010). Because the clinopyroxene phenocrysts in the mafic volcanic rocks have zoned structures, volume-based percentages were considered when calculating the major element contents of the clinopyroxene phenocrysts. The volumetric percentages of the zones of clinopyroxene phenocrysts were estimated according to the backscattering images (Huang et al., 2010). The volume proportions were core: rim = 3:7 for normal zoned clinopyroxenes, core : mantle : rim = 4:5:1 for reverse zoned clinopyroxenes, and core: mantle : rim = 4:5:1 for clinopyroxenes with green cores. Because olivine and clinopyroxene were the main phenocrysts, the equilibrated magma was obtained by subtracting the major elements of olivine and clinopyroxene phenocrysts from the major elements of whole rocks.

The temperature and water contents of the equilibrated magmas were calculated using the major elements of low-Al and high-Al amphibole phenocrysts in Machangqing porphyries (Tables C2), following the method of Ridolfi et al. (2010). The equations are summarized as follows:

$$T(^{\circ}C) = -151.487Si^{*} + 2041 \quad (1)$$

$$H_2O_{melt} = 5.215^{[6]}Al * + 12.28 \quad (2)$$

where Si* and $^{[6]}$Al* represent the silicon index and octahedral

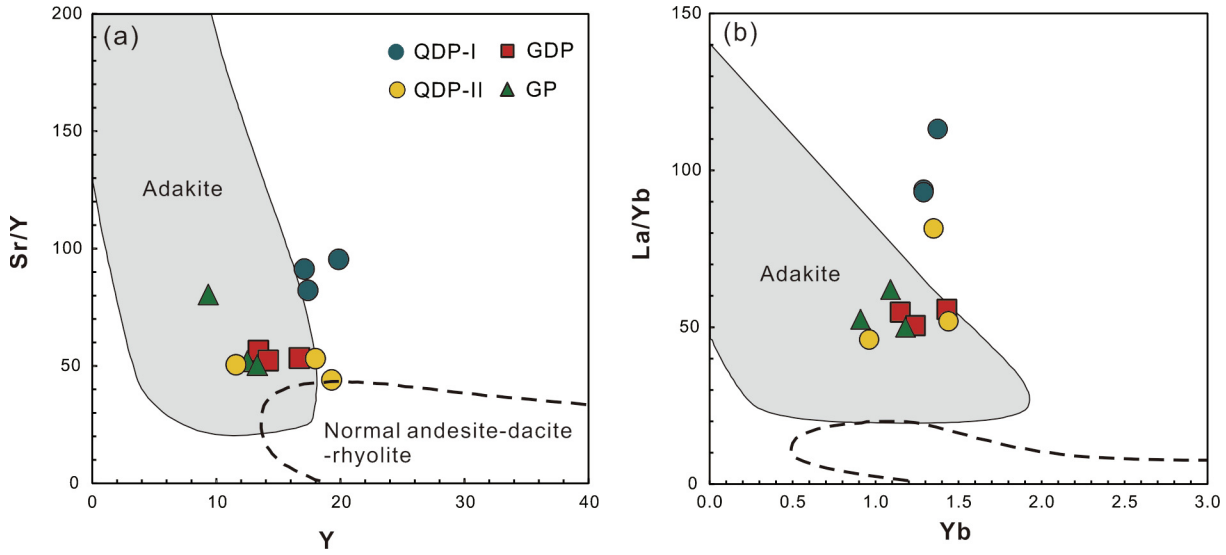

Fig. 7. Plots of (a) Sr/Y vs. Y (Defant and Drummond, 1993) and (b) La/Yb vs. Yb (Castillo et al., 1999) showing that Machangqing intermediate-felsic porphyries are adakite-like rocks.

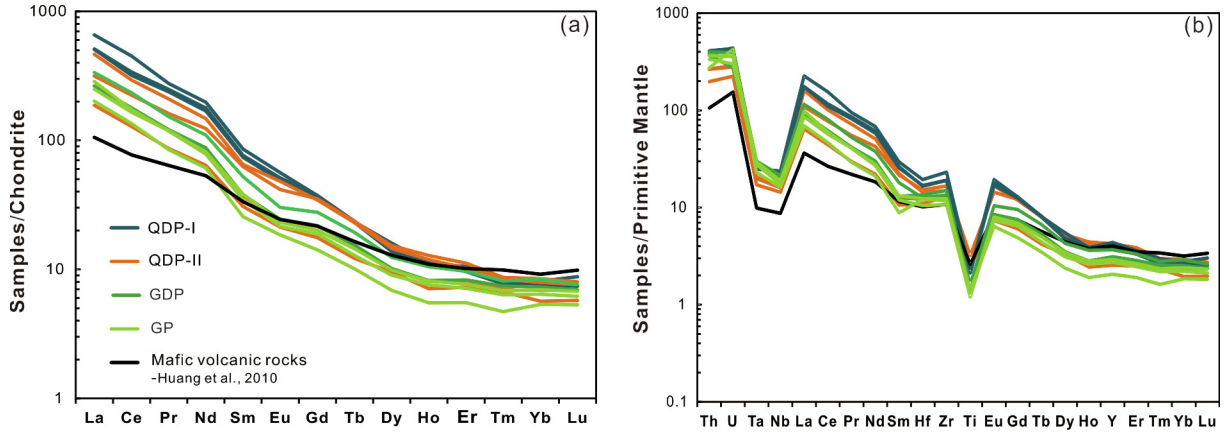

Fig. 8. (a) Chondrite-normalized REE patterns and (b) primitive mantle-normalized multielement diagrams. Chondrite and primitive mantle normalization values are from Sun and McDonough (1989).

aluminum index, respectively (Ridolfi et al., 2010).

High-Al amphiboles in lower crustal xenoliths were used to calculate temperature according to the method described by Ridolfi and Renzulli (2012). The equation is summarized as follows:

$$T(^{\circ}C) = 17098 - 1322.3[Si] - 1035.1[Ti] - 1208.2[Al] - 1230.4[Fe] - 1152.9[Mg] - 130.40[Ca] + 200.54[Na] + 29.408[K] + 24.410\ln P \quad (3)$$

where [] indicates the element content in atoms per formula unit.

We used low-Al amphiboles in Machangqing intermediate-felsic porphyries and high-Al amphiboles in lower crustal xenoliths to calculate pressure, using the method described by Ridolfi and Renzulli (2012). The equation is summarized as follows:

$$\ln P(MPa) = 125.93 - 95876[Si] - 10.116[Ti] - 8.1735[Al] - 9.2261[Fe] - 8.7934[Mg] - 1.6659[Ca] + 2.4835[Na] + 2.5192[K] \quad (4)$$

The method described by Schmidt (1992) was used to calculate pressure using high-Al amphiboles in QDP-I. The equation is summarized as follows:

$$P(kbar) = -3.01 + 4.76[Al] \quad (5)$$

Depth was then calculated using the density of the crust and the mantle, and the obtained pressure. The density is $\rho 1 = 2.7 \times 10^3$ kg/m^3 for depths from the upper to the middle crust (0–30 km) (Kaban et al. 2018; Lucassen et al. 2001), $\rho 2 = 2.86 \times 10^3$ kg/m^3 for depths extending to the lower crust (0–50 km) (Kaban et al. 2018), and $\rho 3 = 3.26 \times 10^3$ kg/m^3 for depths from the lower crust to the upper mantle (50–200 km) (Kaban et al. 2018).

6. Results

6.1. Zircon U–Pb ages

Zircons from the intermediate-felsic porphyries in Machangqing are euhedral and show oscillatory zonation in the CL images (Fig. 5). Twenty-one analyses of zircons from QDP-I yielded $^{206}Pb/^{238}U$ ages from 33.7 to 36.1 Ma, with a weighted mean age of 35.1 ± 0.3 Ma (1σ, MSWD = 2.3) (Fig. 5a). Seventeen analyses of zircons from GDP yielded $^{206}Pb/^{238}U$ ages ranging from 33.7 to 36.4 Ma, with a weighted mean age of 35.2 ± 0.4 Ma (1σ, MSWD = 3.1) (Fig. 5b). Sixteen analyses of zircons from GP yielded $^{206}Pb/^{238}U$ ages ranging from 33.8 to 36.2 Ma, with a weighted mean age of 34.9 ± 0.4 Ma (1σ, MSWD = 1.8) (Fig. 5c). Fifteen analyses of zircons from QDP-II yielded

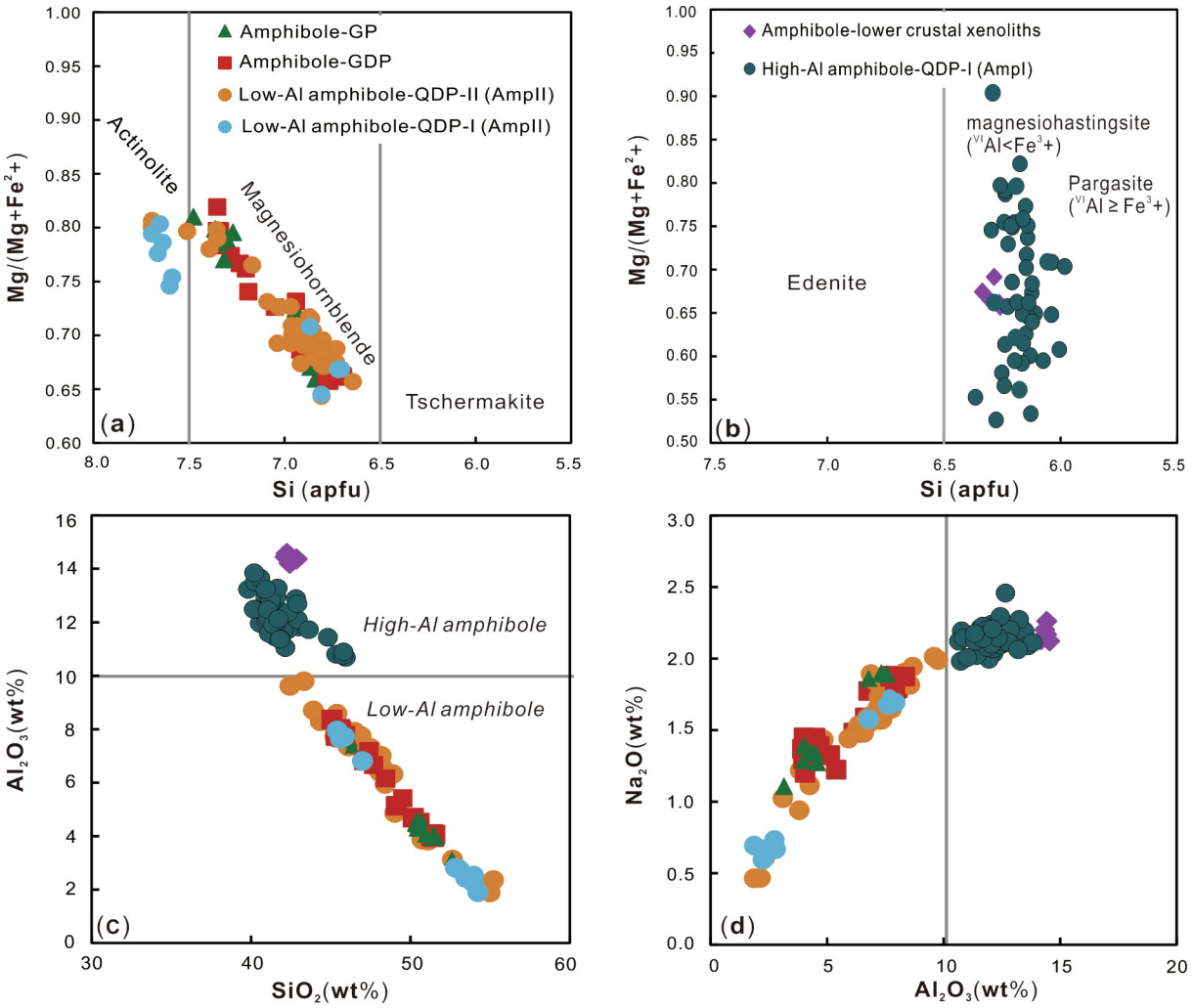

Fig. 9. (a–b) Amphibole classifications after Leake et al. (1997) and (c–d) variations of major elements of amphiboles. (a) Amphibole with $Ca_B \geq 1.5$ apfu, $(Na + K)_A < 0.50$ apfu, and Ti < 0.50 apfu, and (b) amphibole with $Ca_B \geq 1.5$ apfu, $(Na + K)_A \geq 0.50$ apfu, and $Ca_A < 0.50$ apfu. The high-Al amphibole ($Al_2O_3 > 10$ wt%) in QDP-I is magnesiohastingsite, and that in lower crustal xenoliths is pargasite; apfu, atoms per formula unit.

$^{206}Pb/^{238}U$ ages from 32.8 to 36.1 Ma, with a weighted mean age of 34.2 ± 0.5 Ma (1σ, MSWD = 1.2) (Fig. 5d). Overall, these results suggest that these intermediate-felsic porphyries formed at 35.2 to 34.2 Ma. Detailed data is provided in Tables A1.

6.2. Major and trace elements

The results of the major and trace element analyses of the intermediate-felsic porphyries are listed in Tables B1. The intermediate QDPs (QDP-I and QDP-II) has relatively lower SiO_2 contents (58.16–64.05 wt%) than those of the felsic GDP (69.17–70.39 wt%) and GP (69.54–71.78 wt%). The intermediate QDPs has K_2O (4.63–5.40 wt %) and $K_2O + Na_2O$ (7.79–9.46 wt%) contents similar to those of felsic porphyries (K_2O 3.87–5.51 wt% and $K_2O + Na_2O$ 8.37–9.51 wt%). Thus, QDPs belongs to the alkaline series, but GDP and GP belong to the subalkaline series (Fig. 6a). In the K_2O vs. SiO_2 diagram (Fig. 6b), QDPs shows shoshonitic affinities, whereas GDP and GP are high-K calc-alkaline rocks. QDPs, GDP, and GP have similar Al_2O_3 contents of 13.65–16.47 wt%, 14.83–15.30 wt%, and 14.67–15.66 wt%, respectively. GP has lower CaO contents (1.16–1.48 wt%) than QDPs (2.79–6.83 wt%) and GDP (1.87–2.40 wt%). Thus, QDPs and GDP belong to the metaluminous series, with A/CNK [Al_2O_3/(CaO + Na_2O + K_2O)] molar values ranging from 0.60 to 0.98, whereas GP belongs to the peraluminous series, with A/CNK molar values ranging from 1.01 to 1.07 (Fig. 6c). The intermediate QDPs has higher MgO (2.43–7.26 wt%), TFeO (2.65–4.48 wt%), and P_2O_5 (0.20–0.56 wt%) contents than the felsic porphyries (MgO 0.87–1.25 wt %, TFeO 1.72–2.72 wt%, and P_2O_5 0.14–0.19 wt%).

QDPs, GDP, and GP all show characteristics of high Sr/Y (44–95) and La/Yb (46–113), and low Y (9.36–19.9 ppm) and Yb (0.91–1.44 ppm). These characteristics indicate that the intermediate-felsic porphyries are adakite-like rocks (Fig. 7). Further, these porphyries have weak to no Eu anomalies (Fig. 8a; δEu = 0.80–1.02, where $\delta Eu = Eu_N/[(Sm_N \times Gd_N)^{\wedge}0.5]$), high large ion lithophile elements (e.g., Ba = 862–4310 ppm and Sr = 585–1896 ppm), and relatively low contents of high field-strength elements (e.g., Nb, Ta, Zr, and Hf) (Fig. 8b). Interestingly, the incompatible trace-element patterns of QDP-II are the same as those of GDP and GP (Fig. 8).

6.3. Sr–Nd isotopes

The Sr–Nd isotope data of QDP-I, QDP-II, GDP, and GP are listed in Tables B2. QDP-I and QDP-II have $(^{87}Sr/^{86}Sr)_i$ = 0.7069–0.7076 and εNd(t) = −6.6 to −5.3, which are similar to the values of the felsic GDP and GP, $(^{87}Sr/^{86}Sr)_i$ = 0.7068–0.7069 and εNd(t) = −5.4 to −5.1.

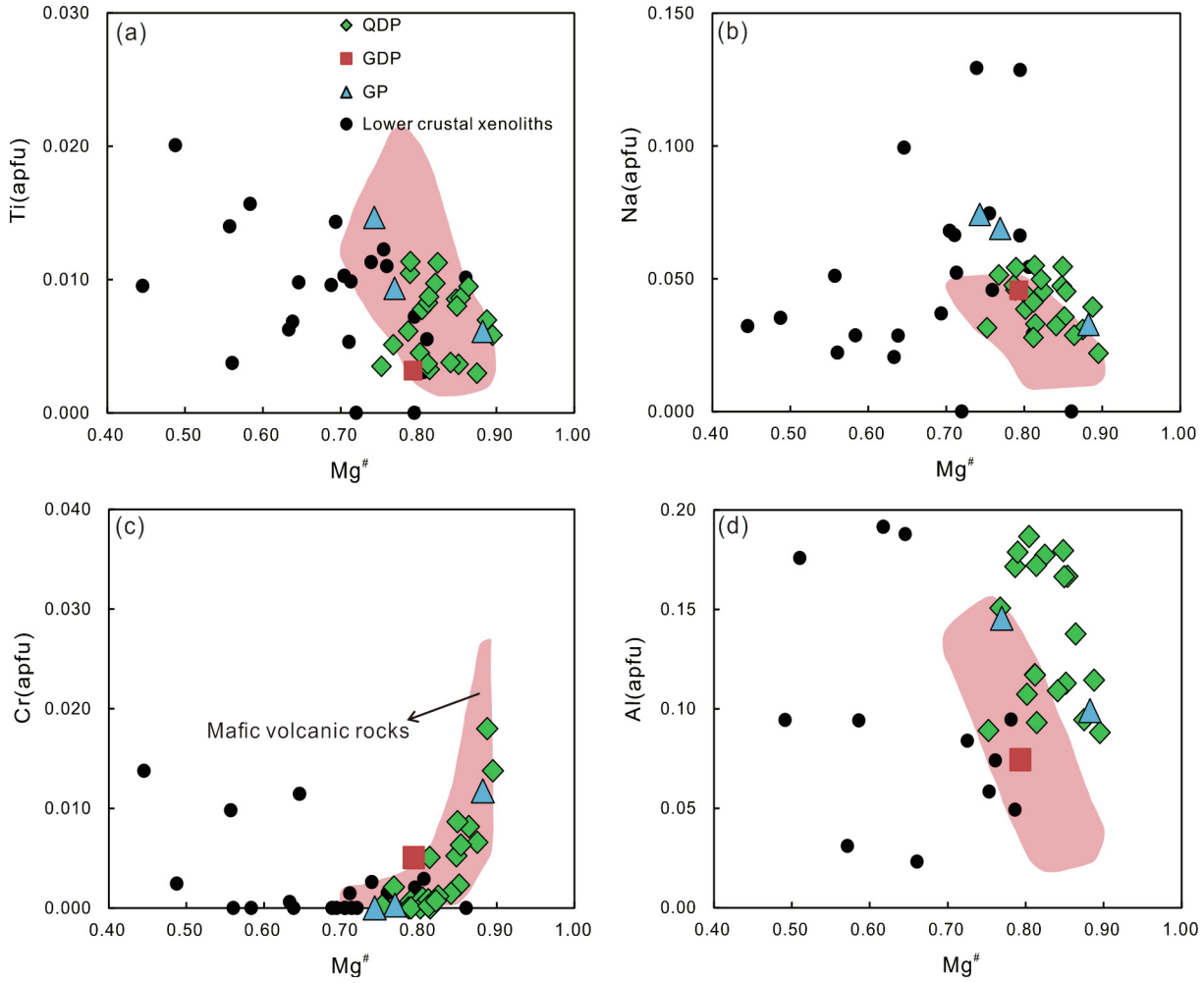

Fig. 10. Variations of major element contents of clinopyroxene antecrysts in QDP-I, GDP, and GP and comparison between clinopyroxene phenocrysts in mafic volcanic rocks (pink area; Huang et al., 2010) and clinopyroxenes in lower crustal xenoliths captured from juvenile mafic lower crust (Wei and Wang, 2004; Zhao et al. 2003; Zhou et al., 2017).

6.4. Mineral geochemistry

6.4.1. Amphiboles

According to amphibole classification (Leake et al., 1997), amphiboles in Machangqing intermediate-felsic porphyries are divided into two groups (Fig. 9a–c): high-Al amphiboles (Al_2O_3 > 10 wt%), including pargasite and magnesiohastingsite, and low-Al amphiboles (Al_2O_3 < 10 wt%), including magnesiohornblende and actinolite. Amphiboles from the lower crustal xenoliths are high-Al pargasite. In QDP-I, AmpI is high-Al magnesiohastingsite and AmpII is low-Al amphibole, including magnesiohornblende and actinolite. QDP-II remains only low-Al magnesiohornblende phenocrysts. Actinolite exists as mafic minerals in the groundmass of QDP-II. GDP and GP only have low-Al magnesiohornblende phenocrysts.

The range of major element contents of high-Al amphiboles in lower crustal xenoliths are concentrated (Fig. 9). The high-Al amphiboles contain 14.20–14.57 wt% Al_2O_3, 2.12–2.26 wt% Na_2O, 42.2–42.9 wt% SiO_2 and 1.68–1.80 wt% K_2O, and 10.53–10.80 wt% CaO. The major element contents of amphiboles in Machangqing intermediate-felsic porphyries (e.g., Al_2O_3, SiO_2, and Na_2O) show linear relationships (Fig. 9c and d). Low-Al amphiboles in QDP-I have major element contents similar to those of low-Al amphiboles in QDP-II, GDP, and GP (Fig. 9). The high-Al amphiboles in QDP-I have higher contents of Al_2O_3 (11.04–13.85 wt%), Na_2O (1.99–2.46 wt%), and K_2O (1.10–2.07 wt%), and lower SiO_2 contents (39.8–43.6 wt%) than those of the low-Al amphiboles in QDP-I, QDP-II, GDP, and GP, which contain Al_2O_3 = 1.87–9.78 wt%, Na_2O = 0.46–2.01 wt%, K_2O = 0.14–1.25 wt %, and SiO_2 = 42.5–55.2 wt%. However, the low-Al amphiboles in the Machangqing porphyries have higher CaO contents (10.96–12.45 wt%) than the high-Al amphiboles in QDP-I (10.24–11.42 wt%).

Because the spot size used for LA-ICP-MS analysis was 32 μm, only low-Al amphiboles in QDP-I, QDP-II, and GDP were analyzed, because of the sufficient width of their zonation and a lack of alterations. The chondrite-normalized REE patterns are shown in Fig. 11a and b. The REE contents of high-Al amphiboles in QDP-I are high, with an average of 583 ppm. The REE patterns of high-Al amphiboles in QDP-I present convex upward shapes (Fig. 11a), with averages of La_N/Yd_N = 15, La_N/Nd_N = 0.8, and Sm_N/Yb_N = 12. These patterns present similar shapes to those of clinopyroxene antecrysts in QDP-I (Fig. 11a). The low-Al amphiboles in QDP-I, QDP-II, and GDP have similar REE contents (average of 315 ppm). The REE patterns of the low-Al amphiboles show weak convex upward shapes (Fig. 11a and b), with averages of La_N/Yd_N = 4, La_N/Nd_N = 0.6, and Sm_N/Yb_N = 4. In comparison with the high-Al amphiboles, the low-Al amphiboles possess distinct negative Eu anomalies (average δEu = 0.60) (Fig. 11a and b). The REE contents of the cores and rims of low-Al amphiboles in GDP are similar (Fig. 11b). Detailed data of the standard samples analyzed by LA-ICP-MS and major and trace elements of the amphiboles are presented in Tables C1–C3.

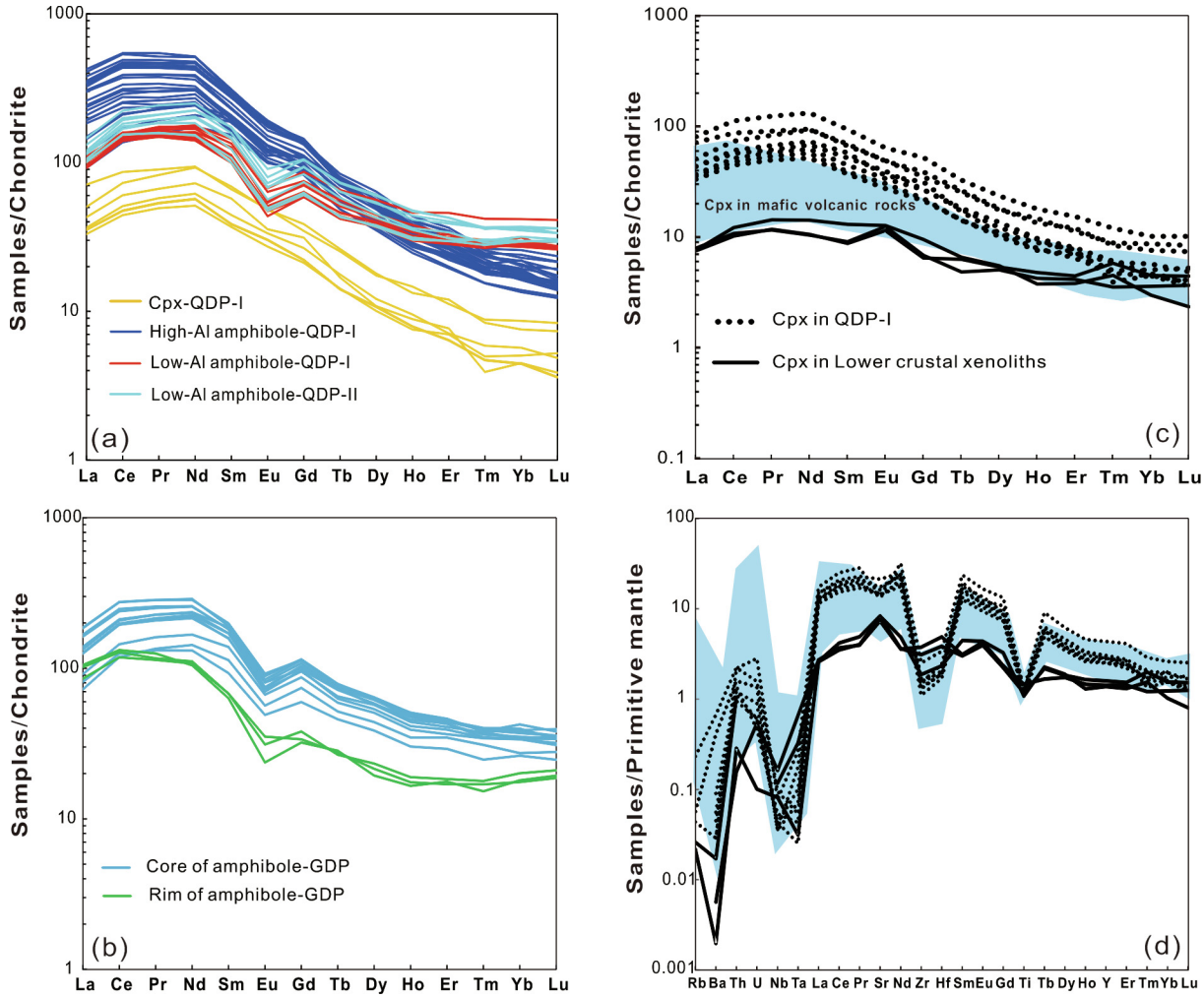

Fig. 11. (a–c) Chondrite-normalized REE patterns of amphiboles and clinopyroxenes; (d) Primitive mantle-normalized multi-element patterns of clinopyroxenes. The data for clinopyroxenes in the mafic volcanic rocks are from Huang et al. (2010).

Table 1
The crystallizing physicochemical conditions of the mafic minerals.

Rock type	Temperature °C	Std.	Avg. °C	Pressure MPa	Std.	Avg. MPa	Depth km	Avg. km	H_2O_m wt.%	Std.
Cpx-Mafic volcanic rocks	1288–1171 [a]	33		2060–590 [a]	0.17		64–22			
Amp-Lower crustal xenoliths	905–932 [b]	24	918	1240–1450 [b]	0.25	1330	44–52	47		
High-Al Amp-QDP-I	894–989 [c]	22	946	634–854 [d]	60	727	24–32	27	3.4–6.0 [c]	0.5–0.9
Low-Al Amp-QDP-I	795–827 [c]	22	815	107–158 [b]	12–18	132	4–6	5	3.7–3.9 [c]	0.4
Low-Al Amp-QDP-II	700–883 [c]	22	799	32–269 [b]	4–31	129	1–10	5	2.9–4.5 [c]	0.4
Low-Al Amp-GDP	718–833 [c]	22	773	45–174 [b]	5–20	104	2–7	4	3.0–4.2 [c]	0.4
Low-Al Amp-GP	706–813 [c]	22	759	34–107 [b]	4–20	93	1–6	4	3.1–4.4 [c]	0.4

a, Methods are from Purika et al. (2003); b, Methods are from Ridolfi and Renzulli (2012); c, Methods are from Ridolfi et al. (2010); d, Methods are from Schmidt (1992). Corresponding density of lithosphere are $\rho_1 = 2.7 \times 10^3$ kg/m^3 for depth 0–30 km; $\rho_2 = 2.86 \times 10^3$ kg/m^3 for depth 0–50 km; $\rho_3 = 3.26 \times 10^3$ kg/m^3 for depth 50–200 km. Density data are from Kaban et al. (2018) and Lucassen et al.(2001). Avg., average.

6.4.2. Clinopyroxene

The major element contents of the clinopyroxene antecrysts in the Machangqing intermediate-felsic porphyries are similar to each other (Fig. 10). Clinopyroxene antecrysts in QDP-I have $Mg^{\#}$ = 75–90. The contents of MgO, TFeO, Al_2O_3, TiO_2, and Na_2O are 14.07–18.56 wt%, 3.87–8.25 wt%, 2.04–5.14 wt%, 0.11–0.40 wt%, and 0.31–0.77 wt%, respectively. The Ti/Al values of the clinopyroxene antecrysts in QDP-I are 0.03–0.07. The clinopyroxene antecrysts in GDP and GP have MgO, TFeO, Al_2O_3, TiO_2, Na_2O, and Ti/Al contents similar to those in QDP-I: 13.89–18.86 wt%, 4.48–8.56 wt%, 1.72–4.61 wt%, 0.11–0.52 wt%, 0.46–1.02 wt%, and 0.04–0.07, respectively.

The chondrite-normalized REE patterns and primitive mantle-normalized trace-element patterns of clinopyroxenes in QDP-I and lower crustal xenoliths are presented in Fig. 11c and d. The total REE contents of clinopyroxenes (average of 22 ppm) from the lower crustal xenoliths are lower than those from QDP-I (average of 103 ppm). The clinopyroxenes from the lower crustal xenoliths have flat REE patterns (average La_N/Yb_N = 2; Fig. 11c), whereas the REE patterns of the clinopyroxenes in QDP-I show convex upward shapes (Fig. 11c), with averages of La_N/Yb_N = 8, La_N/Nd_N = 0.6, and Sm_N/Yb_N = 9. The primitive mantle-normalized trace-element patterns of clinopyroxenes in QDP-I show distinctive negative Sr, Zr, Hf, and Ti anomalies, in contrast to those of

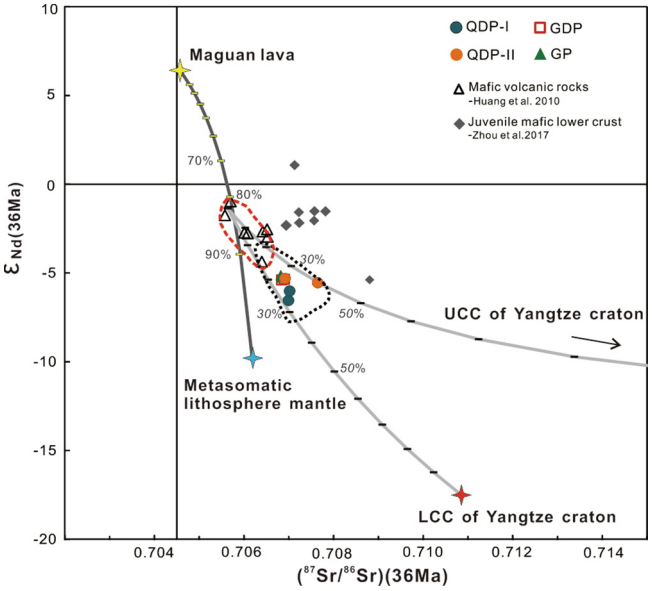

Fig. 12. Initial Sr–Nd isotope model. The black dashed line represents the published data for Machangqing porphyries (Bi et al., 2005; Lu et al., 2013; Tong et al., 2019); the red dashed line represents the range of the Eocene mafic volcanic rock from Huang et al. (2010). Depleted magmas derived from the asthenosphere are represented by Neogene Maguan lava [$(^{87}Sr/^{86}Sr)_i$ = 0.7046, Sr = 642 ppm, εNd(t) = 6.4, Nd = 38.4 ppm] in southeastern Yunnan (Xia and Xu 2004), and the metasomatic lithosphere mantle metamorphosed by Neoproterozoic oceanic subduction is represented by Neoproterozoic mafic dikes (Zhao and Asimow, 2018), and the average values are used [$(^{87}Sr/^{86}Sr)_i$ = 0.7062, Sr = 360 ppm, εNd(t) = −9.8, and Nd = 7.5 ppm]. Data for the lower crust of the Yangtze Craton (LCC) [$(^{87}Sr/^{86}Sr)_i$ = 0.7108, Sr = 854 ppm, εNd(t) = −17.5, Nd = 30.1 ppm] and the upper crust of Yangtze Craton (UCC) [$(^{87}Sr/^{86}Sr)_i$ = 0.7223, Sr = 220 ppm, εNd(t) = −11.7, and Nd = 24.3 ppm] are from Chen and Jahn (1998).

clinopyroxenes in lower crustal xenoliths, which have obvious positive Sr and weak negative Ti anomalies, but no Zr or Hf anomalies (Fig. 11d). Detailed geochemical data of the clinopyroxenes are presented in Tables C4 and C5.

6.5. Physicochemical conditions

The crystallizing physicochemical conditions calculated in this work are summarized in Table 1. The errors are ± 22 °C for magma temperature and ± 0.4 wt% for magma water contents (under certain conditions it reached as high as ± 15%) calculated using the method described by Ridolfi et al. (2010). For the temperatures and pressures calculated using the methods of Ridolfi and Renzulli (2012), the errors are ± 23.5 °C and ± 11.5%, respectively. Standard errors of 17 MPa and 33 °C, with no systematic bias, are for the results calculated by the method of Purika et al. (2003). Moreover, actinolites usually crystallize from the deuteric melt, or are products of alteration (Barnes et al., 2016). The lower pressures calculated by actinolites are faulty and are therefore excluded from the results.

The results of crystallization temperatures calculated for the clinopyroxene phenocrysts in the mafic volcanic rocks are 1288 °C; 1221 °C, 1233 °C, 1236 °C; and 1171 °C. The corresponding crystallization pressures and depths are 2060 MPa (64 km); 1380 MPa, 1410 MPa, 1530 MPa (49–55 km); and 590 MPa (22 km). The temperatures calculated for the high-Al amphibole phenocrysts in QDP-I are 894–989 °C, with an average of 945 °C; the pressures are 634–854 MPa, with an average of 727 MPa, the corresponding depths are 24–32 km (average 27 km); the magma water contents (H_2O_m) are 3.4–6.0 wt%. The crystallization conditions calculated for the low-Al amphibole phenocrysts in QDP-I are temperatures of 795–827 °C (average 815 °C), pressures of 107–158 MPa (average pressure 132 MPa, corresponding to a depth of 5 km), and H_2O_m values of 3.7–3.9 wt%. The results calculated for the low-Al amphibole phenocrysts in QDP-II are temperatures of 700–883 °C (average 799 °C), pressures of 32–269 MPa (average 129 MPa, corresponding to a depth of 5 km), and H_2O_m values of 2.9–4.5 wt%. The physicochemical conditions calculated for the low-Al amphibole phenocrysts in GDP are temperatures of 718–833 °C (average 773 °C), pressures of 45–174 MPa (average 104 MPa, corresponding to a depth of 4 km), and H_2O_m values of 3.0–4.2 wt%. The physicochemical conditions calculated for the low-Al amphibole phenocrysts in GP are temperatures of 706–813 °C (average 759 °C), pressures of 34–107 MPa (average 93 MPa, corresponding to a depth of 4 km), and H_2O_m values of 3.1–4.4 wt%. The crystallization conditions calculated for high-Al amphiboles in lower crustal xenoliths are temperatures of 905–932 °C (average 918 °C) and pressures of 1240–1450 MPa (average 1330 MPa), corresponding to depths of 44–52 km (average 47 km).

7. Discussion

7.1. Parental magmas of intermediate-felsic porphyries

The three phases of Eocene Machangqing intermediate-felsic porphyries (QDPs, GDP, and GP) display similar characteristics in terms of ages, whole-rock trace elements, Sr–Nd isotopic compositions, and mineral geochemistry of low-Al amphiboles and clinopyroxene antecrysts. These results indicate that the intermediate-felsic porphyries in Machangqing were generated from the same origin.

The Sr and Nd isotope compositions of Machangqing intermediate-felsic porphyries [$(^{87}Sr/^{86}Sr)_i$ = 0.7069–0.7076, εNd(t) − 5.4 to −5.1] are depleted relative to those of the upper crust [$(^{87}Sr/^{86}Sr)_i$ = 0.7138–0.7490, εNd(t) = −10.1 to −12.4] and the old lower crust [$(^{87}Sr/^{86}Sr)_i$ = 0.7092–0.7108, εNd(t) = −15.9 to −17.5] of the Yangtze Craton (Chen and Jahn, 1998). By contrast, the Sr and Nd isotopic compositions of these Eocene Machangqing intermediate-felsic porphyries are slightly enriched relative to those of the mantle-derived mafic volcanic rocks in the Machangqing area [$(^{87}Sr/^{86}Sr)_i$ = 0.7056–0.7065, εNd(t) = −0.97 to −4.36]. The porphyries have Sr–Nd isotope compositions between those of the mantle-derived mafic volcanic rocks and the crust of the Yangtze Craton, with ~70 wt% components of the mantle-derived mafic volcanic rocks and ~30 wt% components of the crust of the Yangtze Craton (Fig. 12). Given this, we propose that these Eocene Machangqing intermediate-felsic porphyries were predominantly derived from the same source as the mantle-derived mafic volcanic rocks, but with less assimilation of the Yangtze crust. Considering that the Sr and Nd isotope compositions of the juvenile mafic lower crustal xenoliths from the Liuhe syenite in the western Yangtze Craton had a wide range [$(^{87}Sr/^{86}Sr)_i$ = 0.7069–0.7088 and εNd (t) −5.4 to 1.1; Zhou et al., 2017], and that whole-rock isotopes commonly exhibit mixed information regarding the magma source (Wang et al., 2019b), we cannot rule out the possibility that the Eocene Machangqing intermediate-felsic porphyries originated from the juvenile mafic lower crust (Lu et al., 2013) based on the Sr–Nd isotope data alone.

The chemical contents of the phenocrysts of mafic minerals in porphyries or volcanic rocks, e.g., clinopyroxenes and amphiboles, however, can record detailed information regarding the magma origin (Cao et al., 2018a, 2018b; Erdmann et al., 2014). The major and trace elemental features of clinopyroxene antecrysts in QDPs, GDP, and GP are quite different from those of the clinopyroxenes from the lower crustal xenoliths (Figs. 10, 11c, and d). The clinopyroxene antecrysts in QDPs, GDP, and GP have much higher $Mg^{\#}$ (75–90) than clinopyroxenes from the lower crustal xenoliths ($Mg^{\#}$ = 45–86; Wei and Wang, 2004; Zhao et al. 2003; Zhou et al., 2017). However, the major and trace elemental features of clinopyroxene antecrysts in QDPs, GDP, and GP are remarkably similar to those of clinopyroxene phenocrysts in the

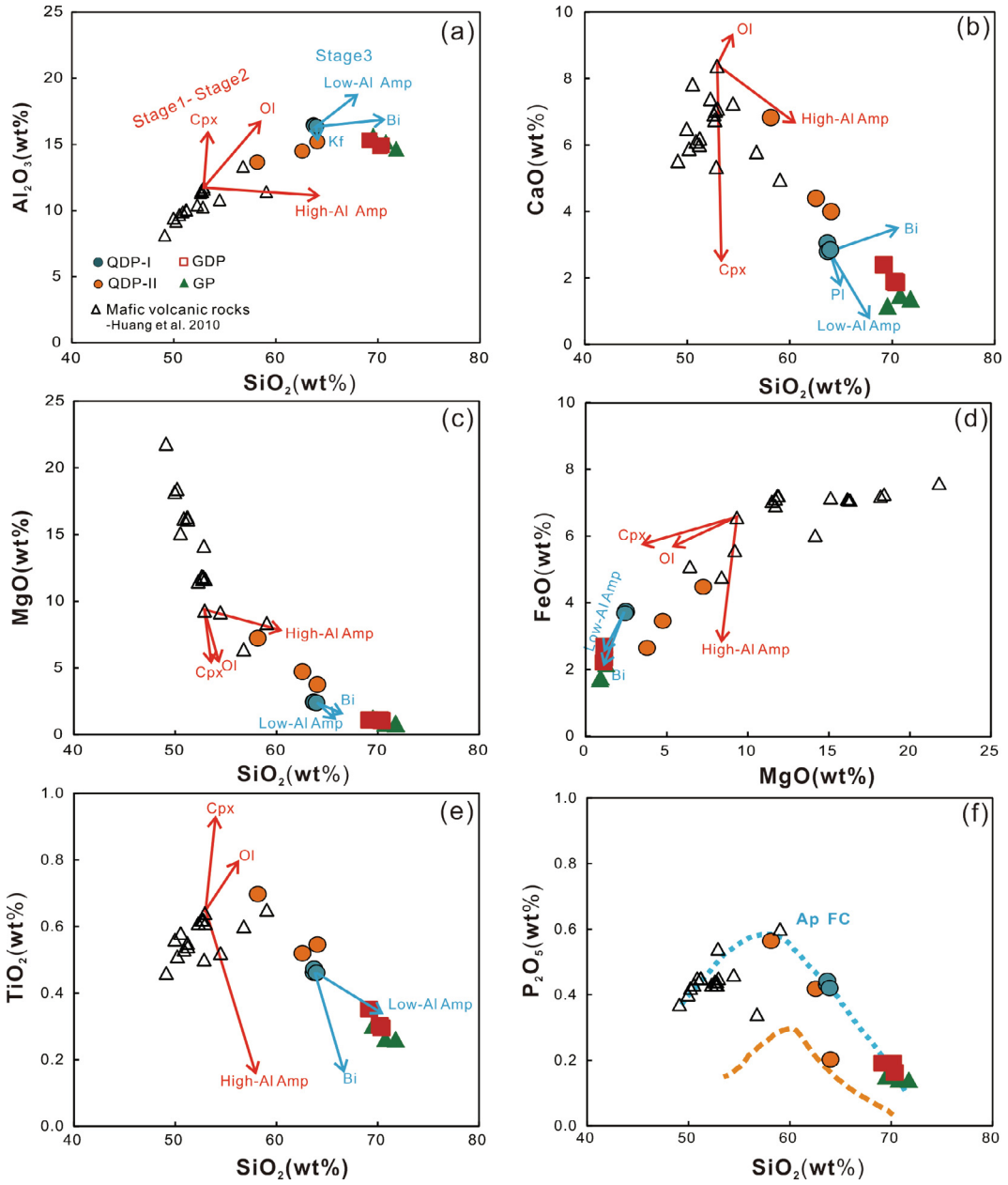

Fig. 13. Harker diagrams showing the major element compositions of whole-rocks and fractional crystallization trends; parameters are listed in Table 2. The orange dotted line is modeled residual liquids formed by equilibrium crystallization of hydrous parental basalts with 4 wt.% H_2O at conditions of 0.3 GPa and 750 °C (Lee and Bachmann, 2014). The evolution trend from this work (blue dotted line) is consistent with the trend presented by the orange line. AP FC, apatite fractional crystallization.

mafic volcanic rocks (Figs. 10 and 11c and d). The clinopyroxene antecrysts in these porphyries have $Mg^{\#}$ of 74–90, Ti/Al ratios of 0.03–0.07, and Na_2O contents of 0.31–1.02 wt%, which are similar to those of clinopyroxene phenocrysts in the mafic volcanic rocks ($Mg^{\#}$ = 77–90, Ti/Al = 0.06–0.16, and Na_2O = 0.22–0.42 wt%; Huang et al., 2010). The REE patterns of the clinopyroxene antecrysts in QDP-I are similar to those of clinopyroxene phenocrysts in the mafic volcanic rocks, and show consistent negative anomalies in Sr, Zr, Hf, and Ti (Fig. 11c and d). The similarities between the clinopyroxenes in the porphyries (QDPs, GDP, and GP) and those in the mafic volcanic rocks suggest that they crystallized from the same mafic magmatic series. Clinopyroxene antecrysts and high-Al amphibole phenocrysts in QDP-I show similar REE patterns (Fig. 11a). Amphiboles and clinopyroxene have similar ratios of the partition coefficients of REEs, i.e., $D_{amp}(La/Sm)/D_{amp}(Eu/Lu) \approx D_{cpx}(La/Sm)/D_{cpx}(Eu/Lu)$, between the minerals and basaltic-dioritic melts (Adam and Green, 2003; Michely et al., 2017; Shimizu et al., 2017). This indicates that the equilibrated magmas of the high-Al amphibole phenocrysts and clinopyroxene antecrysts in QDP-I probably have similar REE patterns, and thus that these magmas belonged to the same magma series. Then, the parental magmas of QDP-I and of the mafic volcanic rocks belong to the same magma series.

In short, the geochemical features of whole rocks and phenocrysts of mafic minerals indicate that Eocene Machangqing intermediate-felsic porphyries were generated from the differentiation of mantle-derived mafic magma with minor crustal assimilation.

7.2. Petrogenesis model

The major elements of whole rocks show fractional crystallization

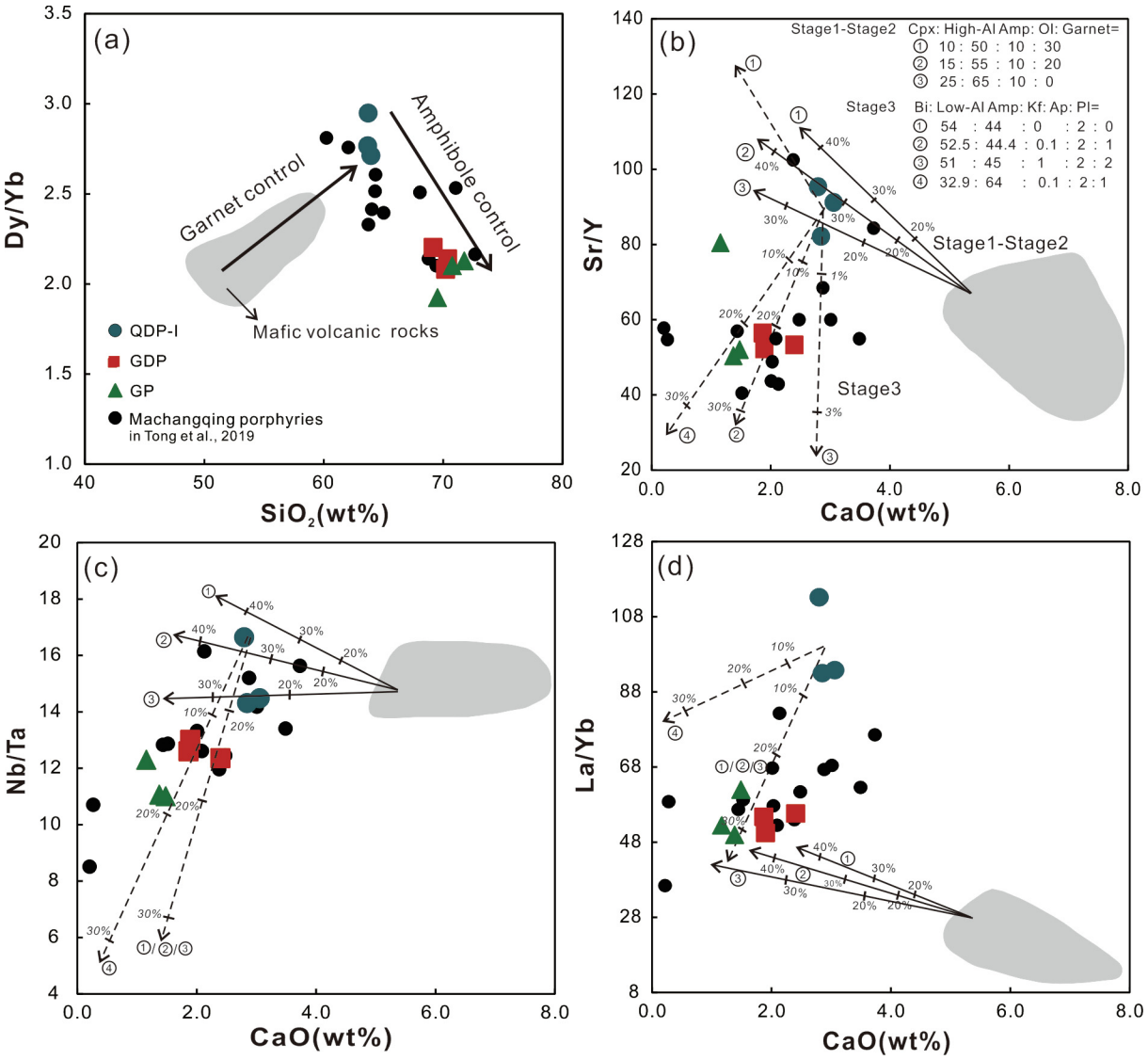

Fig. 14. Simulations of fractional crystallization: (a) Dy/Yb vs. SiO_2 (modified after Davidson et al., 2007); (b) Sr/Y vs. CaO; (c) Nb/Ta vs. CaO; (d) La/Yb vs. CaO. Simulations in (b), (c), and (d) show that from mafic volcanic rocks to intermediate QDP-I, the magma series may have experienced 20–40% fractional crystallization of Ol (olivine), Cpx (clinopyroxene), high-Al Amp (amphibole), and garnet. From intermediate QDP-I to felsic GDP and GP, the proportion of fractional crystallization is 10–30%. The fractionating assemblage mainly consists of Bi (biotite) and low-Al Amp, with minor Kf (alkali-feldspar), Ap (apatite) and Pl (plagioclase).

trends from the mafic volcanic rocks to the felsic porphyries in the Machangqing area (Fig. 13). Particularly, as shown in Fig. 13f, the evolving trend of magma P_2O_5 contents is consistent with the modeled residual liquids formed by the crystallization of hydrous parental basalts (Lee and Bachmann, 2014). The calculated physicochemical conditions of phenocrysts from the intermediate-felsic porphyries and mafic volcanic rocks in the Machangqing area reveal information on the magma source and fractional crystallization processes at different depths of the crust (Fig. 15).

7.2.1. *Partial melting of metasomatic lithosphere mantle*

As mentioned previously, the direction of movement of the Indian plate changed from northeastward to northward at ~40 Ma, followed by clockwise rotation (Replumaz et al., 2014; Xu et al., 2016b). The tectonic regime in the western Yangtze Craton changed from compression to extension during these processes (Fig. 1c and d). The simultaneous southeastward extrusion of the Indochina block, starting at ~41 Ma (Xu et al., 2016b), ultimately absorbed the compression stress exerted on the western Yangtze Craton by the movement of Indian plate. The resultant tectonic transtension may have induced peeling away of the instable lower lithospheric mantle and promoted asthenosphere upwelling in the area of the western Yangtze Craton (He et al., 2016; Lu et al., 2013).

The highest crystallization pressure calculated for clinopyroxene phenocrysts in the mafic volcanic rocks is 2060 MPa, corresponding to a depth of 64 km. This is deeper than the depth of the juvenile mafic lower crust obtained by the calculated physicochemical conditions (1240–1450 MPa, at a depth of 44–52 km). According to seismic tomography studies in Southeastern Tibet (Liu et al., 2001), the pressure is plotted in the range of the upper lithosphere mantle (Fig. 15a). The geothermal gradient of the mafic volcanic rocks is approximately 2.8 °C/km or 0.08 °C/MPa (Fig. 15a). This cooling rate indicates that the mafic magma ascended turbulently through dykes within the crust (Huppert and Sparks, 1985; Fig. 15b). The initial melts of quickly emplaced mafic volcanic rocks comprise components of ~20% asthenospheric and ~80% metasomatic lithospheric magmas (Fig. 12). This indicates that the parental mafic magmas of the Eocene intermediate-felsic porphyries and mafic volcanic rocks in the Machangqing area were derived from partial melting of the enriched lithosphere mantle triggered by asthenosphere upwelling in the Eocene (Fig. 15b).

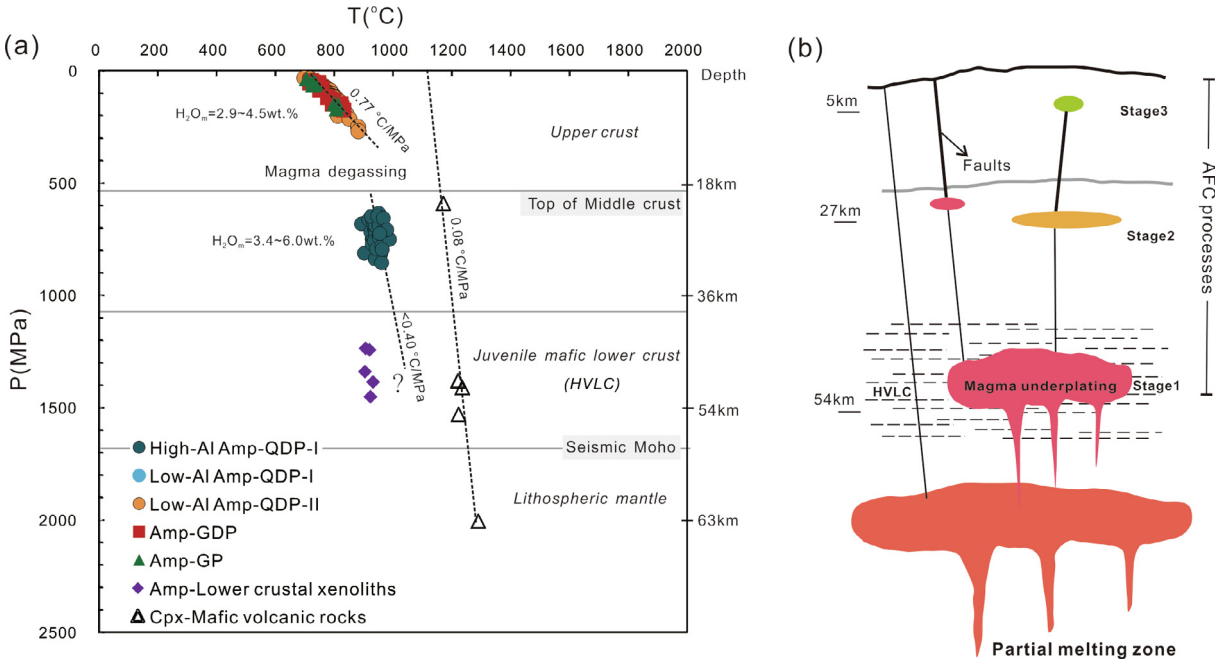

Fig. 15. (a) Variation of physicochemical conditions; the horizontal lines represent borders of the lithosphere structure in the western Yangtze Craton (modified after Liu et al., 2001; Xu et al., 2014; Zhou et al., 2017); the slanted dotted lines are geothermal gradient lines; HVLC, high-velocity lower crust. (b) Schematic diagram for Eocene magmatism in Machangqing.

Table 2
Major and trace elements of single minerals and mineral/melt partition coefficients.

	Ol	Cpx	High-Al amp	garnet	Low-Al amp	Kf	Pl	Bi	Ap
SiO_2 (wt%)	39.70	51.95	41.52		44.04	63.50	59.08	37.19	0.18
Al_2O_3 (wt%)	0.03	1.96	12.33		8.79	20.55	25.70	14.22	0.00
CaO (wt%)	0.32	22.06	10.93	5.0[f]	11.20	2.06	7.42	0.02	54.14
MgO (wt%)	44.73	15.15	11.56		11.20	0.13	0.00	13.89	0.00
FeO (wt%%)	14.59	7.39	15.23		17.07	0.17	0.21	16.93	0.05
TiO_2 (wt.%)	0.03	0.36	1.76		1.46	0.05	0.00	3.21	0.00
P_2O_5 (wt%)	0.00	0.00	0.00		0.00	0.00	0.00	0.00	41.52
La (ppm)		5.36			28.34				
D(La)	0.00003 [a]		0.319 [e]	0.0016 [g]		0.04[b]	0.29[c]	5.713 [d]	7.45[c]
Yb (ppm)		1.27			5.62				
D(Yb)	0.00403 [a]		1.79 [e]	6.6 [g]		0.00525[b]	0.07[c]	1.473 [d]	5.39[c]
Sr (ppm)		180			81.34				
D(Sr)	0.0002 [a]		0.46 [e]	0.0025 [g]		6.75[b]	1.18[c]	0.29[c]	1.31[c]
Y (ppm)		14.5			66.93				
D(Y)	0.0008 [a]		2.47 [e]	3.1 [g]		0.0034[b]	0.04[c]	1.43[c]	10[c]
Nb (ppm)		0.15			27.88				
D(Nb)	0.0005 [a]		0.8 [e]	0.0031 [g]		0.01[b]	0.51[c]	4.01[c]	0.002[c]
Ta (ppm)		0.01			0.60				
D(Ta)	0.0007 [a]		0.75 [e]	0.22[c]		0.033[b]	0.55[c]	1.91[c]	0.002[c]

The calculation formula is based on $C_0 = F^*C_{mineral} + (1 - F)^*C_{melt}$. Major elements of Ol are average value of rim of olivine phenocrysts in mafic volcanic rocks (Huang et al., 2010). Major and trace elements of Cpx are average of clinopyroxene phenocrysts (except green cores) in mafic volcanic rocks (Huang et al., 2010). Major elements and trace elements of high-Al amp and Low-Al amp are averages of high-Al amphibole phenocrysts in QDP-I and low-Al amphibole phenocrysts in Machangqing porphyries. Major elements of Kf and Pl are averages of alkali feldspar and plagioclase phenocrysts in GDP (unpublished data). Major elements of Ap, Bi are average of apatite, biotite phenocrysts in QDP-I (unpublished data). Superscripts a, b, c, d, e and g represent partition coefficients from Melluso et al. (2008), Arzilli et al. (2018), Zhang et al. (2014), Rollinson, 1993, Ma et al. (2016) and Johnson (1998). Superscript f means the major elements of garnet reference contents from Keshav et al. (2007).

7.2.2. *Multi-stage fractional crystallization*

Based on seismic tomography studies, the crust under the Machangqing area are thickened to 52–56 km (Li et al., 2018). The base of the lower crust consists of a juvenile mafic lower crust (high-velocity lower crust, on average 20 km thick), and the upper boundary of the middle crust lays at approximately 20 km (Liu et al., 2001). This structure is further confirmed by the calculated crystallization pressure of the high-Al amphiboles in the lower crustal xenoliths from the Liuhe area (Table 1), 1240–1450 MPa, corresponding to depths of 44–52 km.

The clinopyroxene geobarometer show that the clinopyroxene phenocrysts in the mafic volcanic rocks crystallized from mafic magma at pressures of 1380–1530 MPa, corresponding to depths of 49–55 km (Fig. 15a). These results indicate that the mantle-derived initial mafic magmas underplated at the base of the lower crust in the western Yangtze Craton (stage 1; Fig. 15b). Clinopyroxene and olivine may have crystallized during this process because phenocrysts of these two minerals are commonly formed in mafic volcanic rocks (Huang et al., 2010). In addition, the positive correlations of the whole-rock Dy/Yb values and silica contents between the mafic volcanic rocks and the intermediate QDP-I (Fig. 14a) indicate that garnet may also have

fractionally crystallized from the underplated mafic magma (Davidson et al. 2007).

The calculated crystallization pressure of the high-Al amphibole phenocrysts in QDP-I (Fig. 15a) show that they crystallized at pressures of 854–590 MPa, corresponding to depths of 32–22 km (average 27 km) within the middle crust (Fig. 15b). This indicates another stage of crystallization (stage 2) of the magmas in the middle crust. The diagrams of major elements versus silica for whole rocks (Fig. 13) show that from the mafic magma to the intermediate magma (from stage 1 to stage 2), olivine, clinopyroxene, and high-Al amphibole fractionated from the magmas. The detailed simulations suggested that 20–40% fractional crystallization probably occurred in these two stages, and that the possible mineral assemblage is clinopyroxene (15%), high-Al amphiboles (55%), olivine (10%), and garnet (20%) (Fig. 14b and c).

The low-Al amphibole phenocrysts in the Machangqing porphyries probably formed in the last stage of fractional crystallization (stage 3) within the upper crust (Fig. 15a), because they display the lowest crystallization temperature and pressure (815–759 ˚C and 132–93 MPa, respectively) relative to the mafic phenocrysts in the first two stages. The fractional crystallization models of the major and trace elements of QDPs, GDP, and GP indicate that the minerals that crystallized from the intermediate melts (represented by QDP-I) in this stage include low-Al amphiboles, biotite, feldspar, and apatite (Figs. 13 and 14). However, only a minor amount of feldspar (alkali feldspar and plagioclase) crystallized from the intermediate melts (Fig. 14b), because there is no obvious Eu anomaly in the Machangqing porphyries (Fig. 8a), and the extremely highly compatibility of Sr compared to Y in feldspar (extremely high D(Sr/Y),Table 2). The felsic GDP and GP are therefore the products of fractional crystallization of the intermediate magma formed through stage 2 to stage 3 (Fig. 15b).

Based on the calculated physicochemical conditions of the equilibrated magmas at these three stages, the geothermal gradient changed dramatically from the middle crust (stage 2) to the upper crust (stage 3). The geothermal gradient from stage 1 to stage 2 would have been 0.40 ˚C/MPa at most (as calculated using the average magma temperature and pressure at the juvenile mafic lower crust and the middle crust; Fig. 15a). In stage 3, the geothermal gradient would have been 0.77 ˚C/MPa (as calculated using the magma pressure and temperature at the upper crust; Fig. 15a). Such a drastic increase in the geothermal gradient would probably have induced magma degassing at stage 2, regardless of whether or not the magma was saturated with water (Cashman, 2004; Fiege et al., 2014). Magma degassing can concentrate fluid at the top of the magma chamber, and at the same time can cause increased fractionation of La relative to Yb into the produced hydrous melts (Michard et al., 1983; Tsay et al., 2014). These hydrous magmas with low density and viscosity can ascend easily from the middle crust to the upper crust. Moreover, the fluid may carry Cu and Au to the upper crust for porphyry mineralization.

8. Conclusions

(1) The Eocene Machangqing intermediate-felsic porphyries were initially derived from partial melting of the enriched lithosphere mantle. At ~40 Ma, extension in the western Yangtze Craton caused lower lithosphere mantle delamination, promoted asthenosphere upwelling, and induced melting of enriched lithospheric mantle at a depth of ~64 km. Ascending from the partial melting zone, the initial mafic magma underplated at the base of the lower crust before further evolution through the crust.

(2) Three stages of fractional crystallization of the mantle-derived initial mafic magma are proposed for the genesis of the Eocene Machangqing intermediate-felsic porphyries. Stage 1 occurred at the base of the juvenile mafic lower crust (depth of 49–55 km), followed by stage 2, the fractional crystallization of olivine, clinopyroxene, high-Al amphiboles, and garnet at the middle crust (~27 km), generating magmas with intermediate compositions (roughly represented by QDP-I). Finally, the intermediate magma produced the felsic GDP and GP at the upper crust by fractionation of predominantly low-Al amphiboles and biotite. Magma degassing may have occurred in stage 2 due to a drastic increase in the geothermal gradient. This process induced the parental magmas of QDPs, GDP, and GP to rise from the middle crust to the upper crust, and the separated fluid may have concentrated and carried metals from the magma chamber for mineralization.

CRediT authorship contribution statement

Ying-Jing Wang: Conceptualization, Investigation, Writing - original draft. **Xin-Song Wang:** Conceptualization, Investigation, Writing - review & editing. **Xian-Wu Bi:** Supervision, Project administration, Funding acquisition, Writing - review & editing. **Yan Tao:** Investigation. **Ting-Guang Lan:** Visualization.

Declaration of Competing Interest

The authors declare that they have no known competing financial interests or personal relationships that could have appeared to influence the work reported in this paper.

Acknowledgments

We acknowledge support from National Natural Science Foundation of China [91955209], 100 level innovative talent project of Guizhou province to Xian-Wu Bi, CAS/SAFEA International Partnership Program for Creative Research Teams (Intraplate Mineralization Research Team, KZZD-EW-TZ-20), and Natural Science Foundation of China [41603052, 41873052]. We acknowledge Prof. Chu-Si Li and Prof. Jian-Feng Gao for professional consultation. We appreciate the instructive discussions of Dr. Hai-Hao Guo, Dr. You-Wei Chen, and Dr. Ting Zhou. We are grateful for the constructive reviews from the two anonymous referees, which helped improve this manuscript, and for the editorial assistance of editors Mei-Fu Zhou, Wen-Chang Li, and Jia-Xi Zhou.

Appendix A. Supplementary material

Supplementary data to this article can be found online at https://doi.org/10.1016/j.jseaes.2020.104364.

References

Adam, J., Green, T., 2003. The influence of pressure, mineral composition and water on trace element partitioning between clinopyroxene, amphibole and basanitic melts. Eur. J. Mineral. 15, 831–841.

Arzilli, F., Fabbrizio, A., Schmidt, M.W., Petrelli, M., Maimaiti, M., Dingwell, D.B., Paris, E., Burton, M., Carroll, M.R., 2018. The effect of diffusive re-equilibration time on trace element partitioning between alkali feldspar and trachytic melts. Chem. Geol. 495, 50–66.

Barnes, C.G., Berry, R., Barnes, M.A., Ernst, W.G., 2017. Trace element zoning in hornblende: Tracking and modeling the crystallization of a calc-alkaline arc pluton. Am. Mineral. 102, 2390–2405.

Barnes, C.G., Ernst, W.G., Berry, R., Tsujimori, T., 2016. Petrology and geochemistry of an upper crustal pluton: a view into crustal-scale magmatism during arc to retro-arc transition. J. Petrol. 57, 1361–1388.

Bi, X.W., 1999. Study on alkali-rich intrusive rocks and their relation with metallogenesis of copper and gold in the "Sanjiang" region, western Yunnan (in Chinese). PhD Diss, Institute of Geochemistry, Chinese Academy of Sciences, Guiyang.

Bi, X.W., Hu, R.Z., Ye, Z.J., Shao, S.X., 2000. Relations between A-type granites and copper mineralization as exemplified by the machangqing Cu deposit. Sci. China Series D-Earth Sci. 43, 93–102.

Bi, X.W., Hu, R.Z., Peng, J.T., Wu, K.X., Su, W.C., Zhang, X.Z., 2005. Geochemical characteristics of the Yao'an and Machangqing alkaline-rich intrusions. Acta Petrol. Sin. 21, 113–124.

Bi, X.W., Hu, R.Z., Hanley, J., Mungall, J., Peng, J.T., Shang, L.B., Wu, K.X., Suang, Y.A., Li, H.L., Hu, X.Y., 2009. Crystallisation conditions (T, P, fO(2)) from mineral chemistry of Cu- and Au-mineralised alkaline intrusions in the Red River-Jinshajiang alkaline igneous belt, western Yunnan Province, China. Mineral. Petrol. 96, 43–58.

Cao, M.J., Evans, N.J., Hollings, P., Cooke, D.R., McInnes, B.I.A., Qin, K.Z., Li, G.M., 2018a. Phenocryst zonation in porphyry-related rocks of the Baguio district, Philippines: evidence for magmatic and metallogenic processes. J. Petrol. 59, 825–847.
Cao, M.J., Hollings, P., Cooke, D.R., Evans, N.J., McInnes, B.I.A., Qin, K.Z., Li, G.M., Sweet, G., Baker, M., 2018b. Physicochemical Processes in the Magma Chamber under the Black Mountain Porphyry Cu-Au Deposit, Philippines: Insights from Mineral Chemistry and Implications for Mineralization. Econ. Geol. 113, 63–82.
Cashman, K.V., 2004. Volatile controls on magma ascent and eruption. In: Sparks, R.S.J., Hawkesworth, C.J. (Eds.), State of the Planet: Frontiers and Challenges in Geophysics. Amer Geophysical Union, Washington, pp. 109–124.
Castillo, P.R., Janney, P.E., Solidum, R.U., 1999. Petrology and geochemistry of Camiguin Island, southern Philippines: insights to the source of adakites and other lavas in a complex arc setting. Contrib. Mineral. Petrol. 134, 33–51.
Chen, B., Jahn, B.M., Suzuki, K., 2013. Petrological and Nd-Sr-Os isotopic constraints on the origin of high-Mg adakitic rocks from the North China Craton: Tectonic implications. Geology 41, 91–94.
Chen, F., Li, Q., Li, C., Li, X., Wang, X., Wang, F., 2005. Prospect of High Precision Mass Spectrometer in Isotope Geochemistry. Earth Sci. 30, 639–645.
Chen, J.F., Jahn, B.M., 1998. Crustal evolution of southeastern China: Nd and Sr isotopic evidence. Tectonophysics 284, 101–133.
Chung, S.L., Cheng, H., Jahn, B.M., Oreilly, S.Y., Zhu, B.Q., 1997. Major and trace element, and Sr-Nd isotope constraints on the origin of Paleogene volcanism in South China prior to the South China sea opening. Lithos 40, 203–220.
Chung, S.L., Chu, M.F., Zhang, Y.Q., Xie, Y.W., Lo, C.H., Lee, T.Y., Lan, C.Y., Li, X.H., Zhang, Q., Wang, Y.Z., 2005. Tibetan tectonic evolution inferred from spatial and temporal variations in post-collisional magmatism. Earth-Sci. Rev. 68, 173–196.
Chung, S.L., Jahn, B.M., 1995. Plume-lithosphere Interaction in generation of the Emeishan flood basalts at the Permian-Triassic boundary. Geology 23, 889–892.
Dahren, B., Troll, V.R., Andersson, U.B., Chadwick, J.P., Gardner, M.F., Jaxybulatov, K., Koulakov, I., 2012. Magma plumbing beneath Anak Krakatau volcano, Indonesia: evidence for multiple magma storage regions. Contrib. Mineral. Petrol. 163, 631–651.
Davidson, J., Turner, S., Handley, H., Macpherson, C., Dosseto, A., 2007. Amphibole "sponge" in arc crust? Geology 35, 787–790.
Defant, M.J., Drummond, M.S., 1990. Derivation of some modern arc magmas by melting of young subducted lithosphere. Nature 347, 662–665.
Defant, M.J., Drummond, M.S., 1993. MOUNT-ST-HELENS – Potential example of the partial melting of the subducted lithosphere in a volcanic arc. Geology 21, 547–550.
Elhlou, S., Belousova, E., Griffin, W.L., Pearson, N.J., O'Reilly, S.Y., 2006. Trace element and isotopic composition of GJ-red zircon standard by laser ablation. Geochim. Cosmochim. Acta 70, A158.
Erdmann, S., Martel, C., Pichavant, M., Kushnir, A., 2014. Amphibole as an archivist of magmatic crystallization conditions: problems, potential, and implications for inferring magma storage prior to the paroxysmal 2010 eruption of Mount Merapi, Indonesia. Contrib. Mineral. Petrol. 167, 23.
Fiege, A., Holtz, F., Cichy, S.B., 2014. Bubble formation during decompression of andesitic melts. Am. Mineral. 99, 1052–1062.
Fu, Y., Sun, X.M., Hollings, P., Li, D.F., Yang, T.J., 2018. Geochronology and trace element geochemistry of titanite in the Machangqing Cu-Mo-dominated polymetallic deposit, Yunnan Province, southwest China. J. Asian Earth Sci. 158, 398–414.
Gao, S., Ling, W.L., Qiu, Y.M., Lian, Z., Hartmann, G., Simon, K., 1999. Contrasting geochemical and Sm-Nd isotopic compositions of Archean metasediments from the Kongling high-grade terrain of the Yangtze craton: Evidence for cratonic evolution and redistribution of REE during crustal anatexis. Geochim. Cosmochim. Acta 63, 2071–2088.
Guo, Z.F., Hertogen, J., Liu, J.Q., Pasteels, P., Boven, A., Punzalan, L., He, H.Y., Luo, X.J., Zhang, W.H., 2005. Potassic magmatism in western Sichuan and Yunnan Provinces, SE Tibet, China: Petrological and geochemical constraints on petrogenesis. J. Petrol. 46, 33–78.
He, B., Xu, Y.G., Chung, S.L., Xiao, L., Wang, Y., 2003. Sedimentary evidence for a rapid, kilometer-scale crustal doming prior to the eruption of the Emeishan flood basalts. Earth Planet. Sci. Lett. 213, 391–405.
He, W.Y., Mo, X.X., Yang, L.Q., Xing, Y.L., Dong, G.C., Yang, Z., Gao, X., Bao, X.S., 2016. Origin of the Eocene porphyries and mafic microgranular enclaves from the Beiya porphyry Au polymetallic deposit, western Yunnan, China: Implications for magma mixing/mingling and mineralization. Gondwana Res. 40, 230–248.
Hou, Z.Q., Gao, Y.F., Qu, X.M., Rui, Z.Y., Mo, X.X., 2004. Origin of adakitic intrusives generated during mid-Miocene east-west extension in southern Tibet. Earth Planet. Sci. Lett. 220, 139–155.
Hou, Z.Q., Zeng, P.S., Gao, Y.F., Du, A.D., Fu, D.M., 2006. Himalayan Cu-Mo-Au mineralization in the eastern Indo-Asian collision zone: constraints from Re-Os dating of molybdenite. Miner. Deposita 41, 33–45.
Hou, Z.Q., Zhou, Y., Wang, R., Zheng, Y.C., He, W.Y., Zhao, M., Evans, N.J., Weinberg, R.F., 2017. Recycling of metal-fertilized lower continental crust: Origin of non-arc Au-rich porphyry deposits at cratonic edges. Geology 45, 563–566.
Hu, R.Z., Burnard, P.G., Bi, X.W., Zhou, M.F., Pen, J.T., Su, W.C., Wu, K.X., 2004. Helium and argon isotope geochemistry of alkaline intrusion-associated gold and copper deposits along the Red River-Jinshajiang fault belt, SW China. Chem. Geol. 203, 305–317.
Hu, R.Z., Burnard, P.G., Turner, G., Bi, X.W., 1998. Helium and Argon isotope systematics in fluid inclusions of Machangqing copper deposit in west Yunnan province, China. Chem. Geol. 146, 55–63.
Hu, J.H., Song, X.Y., He, H.L., Zheng, W.Q., Yu, S.Y., Chen, L.M., Lai, C.K., 2018. Constraints of texture and composition of clinopyroxene phenocrysts of Holocene volcanic rocks on a magmatic plumbing system beneath Tengchong, SW China. J. Asian Earth Sci. 154, 342–353.
Huang, X.L., Niu, Y.L., Xu, Y.G., Chen, L.L., Yang, Q.J., 2010. Mineralogical and Geochemical Constraints on the Petrogenesis of Post-collisional Potassic and Ultrapotassic Rocks from Western Yunnan, SW China. J. Petrol. 51, 1617–1654.
Huppert, H.E., Sparks, R.S.J., 1985. Cooling and contamination of mafic and ultramafic magmas during ascent through continental-crust. Earth Planet. Sci. Lett. 74, 371–386.
Irvine, T.N., Baragar, W.R.A., 1971. Guide To chemical classification of common volcanic rocks. Can. J. Earth Sci. 8, 523–548.
Johnson, K.T.M., 1998. Experimental determination of partition coefficients for rare earth and high-field-strength elements between clinopyroxene, garnet, and basaltic melt at high pressures. Contrib. Mineral. Petrol. 133, 60–68.
Kaban, M.K., El Khrepy, S., Al-Arifi, N., 2018. Density structure and isostasy of the lithosphere in Egypt and their relation to seismicity. Solid Earth 9, 833–846.
Keshav, S., Sen, G., Presnall, D.C., 2007. Garnet-bearing Xenoliths from Salt Lake Crater, Oahu, Hawaii: High-Pressure Fractional Crystallization in the Oceanic Mantle. J. Petrol. 48, 1681–1724.
Leake, B.E., Woolley, A.R., Arps, C.E.S., Birch, W.D., Gilbert, M.C., Grice, J.D., Hawthorne, F.C., Kato, A., Kisch, H.J., Krivovichev, V.G., Linthout, K., Laird, J., Mandarino, J.A., Maresch, W.V., Nickel, E.H., Rock, N.M.S., Schumacher, J.C., Smith, D.C., Stephenson, N.C.N., Ungaretti, L., Whittaker, E.J.W., Guo, Y.Z., 1997. Nomenclature of amphiboles: Report of the subcommittee on amphiboles of the International Mineralogical Association, commission on new minerals and mineral names. Am. Mineral. 82, 1019–1037.
Lee, C.T.A., Bachmann, O., 2014. How important is the role of crystal fractionation in making intermediate magmas? Insights from Zr and P systematics. Earth Planet. Sci. Lett. 393, 266–274.
Leng, C.B., Huang, Q.Y., Zhang, X.C., Wang, S.X., Zhong, H., Hu, R.Z., Bi, X.W., Zhu, J.J., Wang, X.S., 2014. Petrogenesis of the Late Triassic volcanic rocks in the Southern Yidun arc, SW China: Constraints from the geochronology, geochemistry, and Sr-Nd-Pb-Hf isotopes. Lithos 190, 363–382.
Li, L.M., Lin, S.F., Davis, D.W., Xiao, W.J., Xing, G.F., Yin, C.Q., 2014. Geochronology and geochemistry of igneous rocks from the Kongling terrane: Implications for Mesoarchean to Paleoproterozoic crustal evolution of the Yangtze Block. Precambr. Res. 255, 30–47.
Li, J.Y., Shi, B.W., Xu, X.Y., Hu, J.F., 2018. Crustal structure beneath the Sichuan basin and adjacent regions revealed by teleseismic receiver functions. Chin. J. Geophys.-Chin. Ed. 61, 2719–2735.
Liang, H.Y., Campbell, I.H., Allen, C.M., Sun, W.D., Yu, H.X., Xie, Y.W., Zhang, Y.Q., 2007. The age of the potassic alkaline igneous rocks along the Ailao Shan-Red River shear zone: Implications for the onset age of left-lateral shearing. J. Geol. 115, 231–242.
Liu, J.H., Liu, F.T., He, J.K., Chen, H., You, Q.Y., 2001. Study of seismic tomography in Panxi paleorift area of southwestern China - Structural features of crust and mantle and their evolution. Sci. China Series D-Earth Sci. 44, 277–288.
Liu, X.F., Zhan, Z.X., Gao, Z.M., Liu, J.J., Li, C.Y., Su, W.C., 1999. Relationships between magmatism and mineralization of alkaline enriched porphyries and deep-derived enclaves in Liuhe, Yunnan province. Sci. China Series D 29, 413–420.
Liu, Y.S., Gao, S., Hu, Z.C., Gao, C.G., Zong, K.Q., Wang, D.B., 2010a. Continental and Oceanic Crust Recycling-induced Melt-Peridotite Interactions in the Trans-North China Orogen: U-Pb Dating, Hf Isotopes and Trace Elements in Zircons from Mantle Xenoliths. J. Petrol. 51, 537–571.
Liu, Y.S., Hu, Z.C., Gao, S., Gunther, D., Xu, J., Gao, C.G., Chen, H.H., 2008. In situ analysis of major and trace elements of anhydrous minerals by LA-ICP-MS without applying an internal standard. Chem. Geol. 257, 34–43.
Liu, Y.S., Hu, Z.C., Zong, K.Q., Gao, C.G., Gao, S., Xu, J.A., Chen, H.H., 2010b. Reappraisement and refinement of zircon U-Pb isotope and trace element analyses by LA-ICP-MS. Chin. Sci. Bull. 55, 1535–1546.
Lu, Y.J., Kerrich, R., Cawood, P.A., McCuaig, T.C., Hart, C.J.R., Li, Z.X., Hou, Z.Q., Bagas, L., 2012. Zircon SHRIMP U-Pb geochronology of potassic felsic intrusions in western Yunnan, SW China: Constraints on the relationship of magmatism to the Jinsha suture. Gondwana Res. 22, 737–747.
Lu, Y.J., Kerrich, R., Kemp, A.I.S., McCuaig, T.C., Hou, Z.Q., Hart, C.J.R., Li, Z.X., Cawood, P.A., Bagas, L., Yang, Z.M., Cliff, J., Belousova, E.A., Jourdan, F., Evans, N.J., 2013. Intracontinental Eocene-Oligocene Porphyry Cu Mineral Systems of Yunnan, Western Yangtze Craton, China: Compositional Characteristics, Sources, and Implications for Continental Collision Metallogeny. Econ. Geol. 108, 1541–1576.
Lucassen, F., Becchio, R., Harmon, R., Kasemann, S., Franz, G., Trumbull, R., Wilke, H.G., Romer, R.L., Dulski, P., 2001. Composition and density model of the continental crust at an active continental margin-the Central Andes between 21 degrees and 27 degrees S. Tectonophysics 341, 195–223.
Ludwig, K.R., 2001. Users manual for isoplot/ex (rev. 2.49): a geochronological toolkit for Microsoft Excel. Berkeley Geochronol. Center Spec. Publ. 1, 1–55.
Ma, Q., Xu, Y.G., Zheng, J.P., Sun, M., Griffin, W.L., Wei, Y., Ma, L., Yu, X.L., 2016. High-Mg adakitic rocks and their complementary cumulates formed by crystal fractionation of hydrous mafic magmas in a continental crustal magma chamber. Lithos 260, 211–224.
Macpherson, C.G., Dreher, S.T., Thirlwall, M.F., 2006. Adakites without slab melting: High pressure differentiation of island arc magma, Mindanao, the Philippines. Earth Planet. Sci. Lett. 243, 581–593.
Melluso, L., Lustrino, M., Ruberti, E., Brotzu, P., Gomes, C.D.B., Morbidelli, L., Morra, V., Svisero, D.P., D'Amelio, F., 2008. Major- and trace-element composition of olivine, perovskite, clinopyroxene, Cr-Fe-Ti oxides, phlogopite and host kamafugites and kimberlites, Alto Paranaiba, Brazil. Can. Mineral. 46, 19–40.
Michard, A., Albarede, F., Michard, G., Minster, J., Charlou, J., 1983. Rare-earth elements and uranium in high-temperature solutions from East Pacific Rise hydrothermal vent

field (13 N). Nature 303, 795.
Middlemost, E.A.K., 1994. Naming Materials in the Magma Igneous Rock System. Earth-Sci. Rev. 37, 215–224.
Michely, L.T., Leitzke, F.P., Speelmanns, I.M., Fonseca, R.O.C., 2017. Competing effects of crystal chemistry and silicate melt composition on trace element behavior in magmatic systems: insights from crystal/silicate melt partitioning of the REE, HFSE, Sn, In, Ga, Ba, Pt and Rh. Contrib. Mineral. Petrol. 172, 19.
Peltzer, G., Tapponnier, P., 1988. Formation and evolution of strike-slip faults, rifts, and basins during the India-Asia collision-An experimental approach. J. Geophys. Res.-Solid Earth Planets 93, 15085–15117.
Purika, K.D., Mikaelian, H., Ryerson, F., Shaw, H., 2003. New clinopyroxene-liquid thermobarometers for mafic, evolved, and volatile-bearing lava compositions, with applications to lavas from Tibet and the Snake River Plain, Idaho. Am. Mineral. 88, 1542–1554.
Qi, L., Jing, H., Gregoire, D.C., 2000. Determination of trace elements in granites by inductively coupled plasma mass spectrometry. Talanta 51, 507–513.
Ren, L., Liang, H.Y., Bao, Z.W., Zhang, J., Li, K.X., Huang, W.T., 2018. Genesis of the high Sr/Y rocks in Qinling orogenic belt, central China. Lithos 314, 337–349.
Replumaz, A., Capitanio, F.A., Guillot, S., Negredo, A.M., Villasenor, A., 2014. The coupling of Indian subduction and Asian continental tectonics. Gondwana Res. 26, 608–626.
Ribeiro, J.M., Maury, R.C., Gregoire, M., 2016. Are Adakites Slab Melts or High-pressure Fractionated Mantle Melts? J. Petrol. 57, 839–862.
Richards, J.R., Kerrich, R., 2007. Special paper: Adakite-like rocks: Their diverse origins and questionable role in metallogenesis. Econ. Geol. 102, 537–576.
Rickwood, P.C., 1989. Boundary lines within petrologic diagrams which use oxides of major and minor elements. Lithos 22, 247–263.
Ridolfi, F., Renzulli, A., 2012. Calcic amphiboles in calc-alkaline and alkaline magmas: thermobarometric and chemometric empirical equations valid up to 1,130A degrees C and 2.2 GPa. Contrib. Mineral. Petrol. 163, 877–895.
Ridolfi, F., Renzulli, A., Puerini, M., 2010. Stability and chemical equilibrium of amphibole in calc-alkaline magmas: an overview, new thermobarometric formulations and application to subduction-related volcanoes. Contrib. Mineral. Petrol. 160, 45–66.
Rollinson, H.R., 1993. Using Geochemical Data: Evaluation, Presentation, Interpretation. Longman Scientific & Technical, London 1–352.
Schmidt, M.W., 1992. Amphibole composition in tonallite as a function of pressure-An experimental calibration of the Al-in hornblende barometer. Contrib. Mineral. Petrol. 110, 304–310.
Shimizu, K., Liang, Y., Sun, C.G., Jackson, C.R.M., Saal, A.E., 2017. Parameterized lattice strain models for REE partitioning between amphibole and silicate melt. Am. Mineral. 102, 2254–2267.
Sun, S.-S., McDonough, W.F., 1989. Chemical and isotopic systematics of oceanic basalts: implications for mantle composition and processes. Geol. Society, London, Spec. Publ. 42, 313–345.
Tang, G.J., Wang, Q., Wyman, D.A., Chung, S.L., Chen, H.Y., Zhao, Z.H., 2017. Genesis of pristine adakitic magmas by lower crustal melting: A perspective from amphibole composition. J. Geophys. Res.-Solid Earth 122, 1934–1948.
Tang, Y., Liu, J.L., Tran, M.D., Song, Z.J., Wu, W.B., Zhang, Z.C., Zhao, Z.D., Chen, W., 2013. Timing of left-lateral shearing along the Ailao Shan-Red River shear zone: constraints from zircon U-Pb ages from granitic rocks in the shear zone along the Ailao Shan Range, Western Yunnan. China. Int. J. Earth Sci. 102, 605–626.
Tong, X., Zhao, Z., Niu, Y., Zhang, S., Cousens, B., Liu, D., Zhang, Y., Han, M., Zhao, Y., Lei, H., Shi, Q., Zhu, D.-C., Sheikh, L., Lutfi, W., 2019. Petrogenesis and tectonic implications of the Eocene-Oligocene potassic felsic suites in western Yunnan, eastern Tibetan Plateau: Evidence from petrology, zircon chronology, elemental and Sr-Nd-Pb-Hf isotopic geochemistry. Lithos 340–341, 287–315.
Tsay, A., Zajacz, Z., Sanchez-Valle, C., 2014. Efficient mobilization and fractionation of rare-earth elements by aqueous fluids upon slab dehydration. Earth Planet. Sci. Lett. 398, 101–112.
Wang, J., Wang, Q., Dan, W., Yang, J.H., Yang, Z.Y., Sun, P., Qi, Y., Hu, W.L., 2019a. The role of clinopyroxene in amphibole fractionation of arc magmas: Evidence from mafic intrusive rocks within the Gangdese arc, southern Tibet. Lithos 338, 174–188.
Wang, Q., Xu, J.F., Jian, P., Bao, Z.W., Zhao, Z.H., Li, C.F., Xiong, X.L., Ma, J.L., 2006. Petrogenesis of adakitic porphyries in an extensional tectonic setting, dexing, South China: Implications for the genesis of porphyry copper mineralization. J. Petrol. 47, 119–144.
Wang, X.F., Metcalfe, I., Jian, P., He, L.Q., Wang, C.S., 2000. The Jinshajiang-Ailaoshan Suture Zone, China: tectonostratigraphy, age and evolution. J. Asian Earth Sci. 18, 675–690.
Wang, X.S., Bi, X.W., Leng, C.B., Zhong, H., Tang, H.F., Chen, Y.W., Yin, G.H., Huang, D.Z., Zhou, M.F., 2014a. Geochronology and geochemistry of Late Cretaceous igneous intrusions and Mo-Cu-(W) mineralization in the southern Yidun Arc, SW China: Implications for metallogenesis and geodynamic setting. Ore Geol. Rev. 61, 73–95.
Wang, X.S., Hu, R.Z., Bi, X.W., Leng, C.B., Pan, L.C., Zhu, J.J., Chen, Y.W., 2014b. Petrogenesis of Late Cretaceous I-type granites in the southern Yidun Terrane: New constraints on the Late Mesozoic tectonic evolution of the eastern Tibetan Plateau. Lithos 208–209, 202–219.
Wang, X.S., Bi, X.W., Chen, Y.W., Pan, L.C., Xu, L.L., 2019b. Crystal fractionation of contaminated melts and re-melting of newly underplated basaltic crust generated Late Triassic andesitic and dioritic intrusions in the southern Yidun Terrane, SW China. Lithos 342–343, 135–151.
Wang, X.S., Williams-Jones, A.E., Bi, X.W., Hu, R.Z., Xiao, J.F., Huang, M.L., 2019c. Late Cretaceous Transtension in the Eastern Tibetan Plateau: Evidence From Postcollisional A-Type Granite and Syenite in the Changdu Area, China. J. Geophys. Res. Solid Earth 124, 6409–6427.
Wei, Q., Wang, J., 2004. Equilibrium P-T conditions of mafic deep-derived enclaves and its sigificance in Liuhe-Xiangduo area of Eastern Tibet. Adv. Earth Sci. 19, 722–731.
Xia P. and Xu Y.G., 2004. Enrichment of the lithospheric mantle in western Yunnan: Comparative studies of two Cenozoic ultrapotassic volcanic series Science in China. 34, 1118–1128.
Xu, J.F., Shinjo, R., Defant, M.J., Wang, Q., Rapp, R.P., 2002. Origin of Mesozoic adakitic intrusive rocks in the Ningzhen area of east China: Partial melting of delaminated lower continental crust? Geology 30, 1111–1114.
Xu, L.L., Bi, X.W., Hu, R.Z., Zhang, X.C., Su, W.C., Qu, W.J., Hu, Z.C., Tang, Y.Y., 2012. Relationships between porphyry Cu-Mo mineralization in the Jinshajiang-Red River metallogenic belt and tectonic activity: Constraints from zircon U-Pb and molybdenite Re-Os geochronology. Ore Geol. Rev. 48, 460–473.
Xu, Y.G., Huang, X.L., Menzies, M.A., Wang, R.C., 2003. Highly magnesian olivines and green-core clinopyroxenes in ultrapotassic lavas from western Yunnan, China: evidence for a complex hybrid origin. Eur. J. Mineral. 15, 965–975.
Xu, Y.K., Huang, Z.L., Zhu, D., Luo, T.Y., 2014. Origin of hydrothermal deposits related to the Emeishan magmatism. Ore Geol. Rev. 63, 1–8.
Xu, Z., Huang, Z., Wang, L., Xu, M., Ding, Z., Wang, P., Mi, N., Yu, D., Li, H., 2016a. Crustal stress field in Yunnan: implication for crust-mantle coupling. Earthq. Sci. 29, 105–115.
Xu, Z., Wang, Q., Li, Z., Li, H., Cai, Z., Liang, F., Dong, H., Cao, H., Chen, X., Huang, X., Wu, C., Xu, C., 2016b. Indo-Asian Collision: Tectonic Transition from Compression to Strike Slip. Acta Geol. Sin. 90, 1–23.
Yu, G.J., 1988. A preliminary study on geological conditions of metallogenesis and genesis of Machangqing gold deposit. J. Kunming Instit. Technol. 13, 1–10 (in Chinese).
Zhang, J., Humphreys, M.C.S., Cooper, G.F., Davidson, J.P., Macpherson, C.G., 2017. Magma mush chemistry at subduction zones, revealed by new melt major element inversion from calcic amphiboles. Am. Mineral. 102, 1353–1367.
Zhang, J.Y., Ma, C.Q., Zhang, C., Li, J.W., 2014. Fractional crystallization and magma mixing: evidence from porphyritic diorite-granodiorite dykes and mafic microgranular enclaves within the Zhoukoudian pluton, Beijing. Mineral. Petrol. 108, 777–800.
Zhao, J.H., Asimow, P.D., 2018. Formation and Evolution of a Magmatic System in a Rifting Continental Margin: Neoproterozoic Arc- and MORB-like Dike Swarms in South China. J. Petrol. 59, 1811–1844.
Zhao, J.H., Zhou, M.F., Wu, Y.B., Zheng, J.P., Wang, W., 2019. Coupled evolution of Neoproterozoic arc mafic magmatism and mantle wedge in the western margin of the South China Craton. Contrib. Mineral. Petrol. 174, 16.
Zhao, X., Mo, X., Yu, X., Lu, B., Zhagn, J., 2003. Mineralogical Characteristics and petrogenesis of deep-derivde xenoliths in cenozoic syeniteporphyry in liuhe, western yunnan province. Earth Sci. Front. 10, 93–104.
Zhong, H., Qi, L.A., Hu, R.Z., Zhou, M.F., Gou, T.Z., Zhu, W.G., Liu, B.G., Chu, Z.Y., 2011. Rhenium-osmium isotope and platinum-group elements in the Xinjie layered intrusion, SW China: Implications for source mantle composition, mantle evolution, PGE fractionation and mineralization. Geochim. Cosmochim. Acta 75, 1621–1641.
Zhou, M.F., Yan, D.P., Kennedy, A.K., Li, Y.Q., Ding, J., 2002. SHRIMP U-Pb zircon geochronological and geochemical evidence for Neoproterozoic arc-magmatism along the western margin of the Yangtze Block, South China. Earth Planet. Sci. Lett. 196, 51–67.
Zhou, Y., Hou, Z.Q., Zheng, Y.C., Xu, B., Wang, R., Luo, C.H., 2017. Granulite xenoliths in Liuhe area: Evidence for composition and genetic mechanism of the lower crust from the Neoproterozoic to Cenozoic. Acta Petrol. Sin. 33, 2143–2160.